Draft version January 31, 2022
Typeset using LaTeX default style in AASTeX631

Another Look at Erupting Minifilaments at the Base of Solar X-Ray Polar Coronal "Standard" and "Blowout" Jets

Alphonse C. Sterling,[1] Ronald L. Moore,[1,2] and Navdeep K. Panesar[3,4]

[1] *NASA/Marshall Space Flight Center, Huntsville, AL 35812, USA*
[2] *Center for Space Plasma and Aeronomic Research,*
University of Alabama in Huntsville, Huntsville, AL 35805, USA
[3] *Lockheed Martin Solar and Astrophysics Laboratory, 3251 Hanover Street, Building 252, Palo Alto, CA 94304, USA*
[4] *Bay Area Environmental Research Institute, NASA Research Park, Moffett Field, CA 94035, USA*

ABSTRACT

We examine 21 solar polar coronal jets that we identify in soft X-ray images obtained from the *Hinode*/X-ray telescope (XRT). We identify 11 of these jets as blowout jets and four as standard jets (with six uncertain), based on their X-ray-spire widths being respectively wide or narrow (compared to the jet's base) in the XRT images. From corresponding Extreme Ultraviolet (EUV) images from the Solar Dynamics Observatory's (*SDO*) Atmospheric Imaging Assembly (AIA), essentially all (at least 20 of 21) of the jets are made by minifilament eruptions, consistent with other recent studies. Here, we examine the detailed nature of the erupting minifilaments (EMFs) in the jet bases. Wide-spire ("blowout") jets often have ejective EMFs, but sometimes they instead have an EMF that is mostly confined to the jet's base rather than ejected. We also demonstrate that narrow-spire ("standard") jets can have either a confined EMF, or a partially confined EMF where some of the cool minifilament leaks into the jet's spire. Regarding EMF visibility: we find that in some cases the minifilament is apparent in as few as one of the four EUV channels we examined, being essentially invisible in the other channels; thus it is necessary to examine images from multiple EUV channels before concluding that a jet does not have an EMF at its base. The size of the EMFs, measured projected against the sky and early in their eruption, is $14'' \pm 7''$, which is within a factor of two of other measured sizes of coronal-jet EMFs.

Keywords: Solar filament eruptions, solar corona, solar x-ray emission, solar extreme ultraviolet emission

1. INTRODUCTION

Solar coronal jets are transient features observed at coronal wavelengths, with spires that become long and narrow as they extend outward from the solar surface into the corona. The base of the jets also become bright, and frequently the brightest part is located on one side of the base (a feature that we will call the *jet bright point*, JBP, following Sterling et al. 2015). Interest in jets increased dramatically with X-ray observations from *Yohkoh* (Shibata et al. 1992). In polar coronal holes, a typical coronal jet reportedly will reach a length of ∼50,000 km, have width of ∼8000 km, and live for ∼10 min (Savcheva et al. 2007). In addition to appearing in coronal holes, they also occur in quiet Sun, and at the periphery of active regions. Following the *Yohkoh* studies, they have also been observed in X-rays with the X-Ray Telescope (XRT) on *Hinode* (Cirtain et al. 2007), and they have also been widely studied in EUV (e.g. Nisticò et al. 2009) and at other wavelengths. Several reviews are now available describing historical and recent progress (Shibata & Magara 2011; Raouafi et al. 2016; Hinode Review Team et al. 2019; Innes et al. 2016; Shen 2021).

An early idea for the origin of jets held that they resulted when new magnetic flux emerged from below the photosphere and reconnected with encountered far-reaching coronal field (Shibata et al. 1992). Various numerical simulation studies provided support for this *emerging flux model* for jet production (e.g., Yokoyama & Shibata 1995; Nishizuka et al. 2008; Moreno-Insertis & Galsgaard 2013; Fang et al. 2014). *Yohkoh* images however only detected relatively hot coronal emissions, and the magnetograms of the time were mainly low-cadence (a few per day) from the ground. It turns out that these limitations helped to conceal other important properties of coronal jets.

Subsequent studies of jets over multiple EUV wavelengths, mainly from the Atmospheric Imaging Assembly (AIA) on the Solar Dynamics Observatory (*SDO*) spacecraft, along with continuous full-disk, high-cadence (45 s) magnetograms from the Helioseismic and Magnetic Imager (HMI), also on *SDO*, allowed for a new interpretation of the cause of jets. Some studies of single jets indicated that a jet can result from eruption of a small-scale filament (e.g., Shen et al. 2012; Hong et al. 2014; Adams et al. 2014). Similar single-jet studies showed cases where a jet came from a site where magnetic flux cancelation was occurring, rather than flux emergence (e.g. Shen et al. 2012; Hong et al. 2014; Young & Muglach 2014a,b; Adams et al. 2014). Sterling et al. (2015) proposed what we call a *minifilament eruption model*, whereby essentially all jets result from the eruption of such small-scale filaments, or minifilaments. Here, we will refer to the cool-material erupting minifilament by EMF.

The basic idea is presented in a schematic in Figure 2 of Sterling et al. (2015); a slightly modified version of the same schematic appears in Figure 1 of Sterling et al. (2018), and we will refer to labelings in that version (the same labelings are in Figure 9, below). The schematic is based on Sterling et al. (2015)'s inference that, in a coronal hole consisting of a pervasive magnetic polarity (say, negative) open field, there would be an opposite-polarity (positive) magnetic element embedded at the jet location. (The same picture works for the pervasive field being a foot and leg of a large closed-loop coronal field, as long as the coronal loop is much larger in length and foot diameter than the jet-base bipole embedded inside the foot. Here we discuss the situation in terms of open field, both in order to simplify the discussion, and because the examples we deal with in this paper are in polar coronal holes, where the coronal field is expected to be largely open.) This embedded positive-polarity element would form an anemone-shaped magnetic structure (Shibata et al. 2007), with lobes connecting the positive flux element to the coronal hole's surrounding negative magnetic flux. One lobe of this anemone would contain the minifilament (the lobe connected by magnetic elements labeled M2 and M3 in the schematic shown in Sterling et al. (2018) (those same labels are included in the schematic of Figure 9(a), below), and that minifilament (consisting of both the cool minifilament chromospheric material and the magnetic field/flux rope enveloping and carrying that cool material) would erupt outward. As it does so, two reconnections ensue: One is *external reconnection* between the field enveloping the EMF flux rope and the ambient open coronal field surrounding the anemone. That external reconnection would result in some of the field enveloping the minifilament becoming open. Reconnection-heated material flowing out along that open field would form the jet spire. Also, that external reconnection would add new reconnection-heated loops to the M1—M2 lobe, connecting the positive-polarity element with negative polarity on the far side of that lobe. The other reconnection would be *internal reconnection* among the legs of the enveloping field, occurring below the EMF's flux rope; this would form a closed heated arcade of loops, the JBP, below the EMF, analogous to the flare arcade forming below a typical large-scale erupting filament. Thus, Sterling et al. (2015) argued that coronal jets are scaled-down versions of large-scale magnetic eruptions, that often make eruptions of typically sized filaments, typical solar flares, and coronal mass ejections (CMEs), as in the case of the standard flare model (e.g., Hirayama 1974; Shibata et al. 1995; Moore et al. 2001; Chen 2011). In particular, in this view the JBP forms under the EMF by internal reconnection in the erupting lobe, not by the external reconnection of the emerging lobe, by which the JBP was argued to form in the emerging-flux model (Yokoyama & Shibata 1995). Sterling et al. (2015) found in each of the 20 jets they examined that the JBP formed at the location of the minifilament's eruption onset.

Other studies investigating the eruption mechanism of a selection of quiet Sun and coronal hole jets have also found that they often result from eruptions of a minifilament. This includes work by us (e.g., Panesar et al. 2016b, 2017, 2018; McGlasson et al. 2019). Other groups have also found similar results. For example, Kumar et al. (2019) found that two-thirds of the equatorial coronal hole jets they studied included EMFs; for the remaining one-third of their sample they did not observe erupting cool-material minifilaments, but those events did exhibit other eruptive signatures. So Kumar et al. (2019) concluded that every jet of their study "involved a filament-channel eruption." Other workers have also reported EMFs in quiet Sun and coronal hole single-jet studies (e.g Shen et al. 2017; Doyle et al. 2019; Zhang et al. 2021). Therefore, while we are unable to say whether all quiet Sun and coronal hole jets result from EMFs, there is strong evidence that minifilament eruptions at least often produce such jets. In earlier studies, prior to AIA observations, often EMFs would not have been visible, due to poorer cadenced in the EUV (although even in that case some studies indicated jets resulted from small-scale eruptions; e.g. Nisticò et al. 2009). Because the EMFs are not readily visible in X-ray images (Sterling et al. 2015), it is not surprising that the earliest studies in X-rays without access to quality EUV images (e.g. Shimojo et al. 1996) would not have detected EMFs in X-ray images.

In subsequent studies, Panesar et al. (2016b) argued that the primary process leading to and triggering the minifilament eruptions causing jets is magnetic flux cancelation. Several earlier and later works support this view (e.g., Hong et al. 2011; Huang et al. 2012; Shen et al. 2012; Young & Muglach 2014a; Adams et al. 2014; Sterling et al. 2017; Panesar et al. 2017, 2018; McGlasson et al. 2019; Muglach 2021). Kumar et al. (2019), however, argue that shearing and/or field rotation may be more important than cancelation in many jets.

A series of numerical simulations (Wyper et al. 2017, 2018a,b; Wyper et al. 2019; Doyle et al. 2019) supports the basic concept of the minifilament eruption model. These workers, however, prefer the term “breakout model,” emphasizing the external reconnection, which they argue is essential to triggering the eruption.

The situation for active region jets viz à viz EMFs is less certain. EMFs do make some active region jets (e.g., Joshi et al. 2017; Solanki et al. 2020). There are also studies of active region jets that do not report or observe concurrent EMFs, with examples including Cheung et al. (2015) and Mulay et al. (2016); Mulay et al. (2018), although it is unclear whether those investigators were specifically looking for such features.

Sterling et al. (2016, 2017) also investgated active region jets, and looked to see whether they were consistent with the minifilament-eruption model. Sterling et al. (2016) looked at several jets from a single active region. Each of three of those jets that they examined in detail displayed a clear EMF at the start of the jet, erupting from a magnetic neutral line between opposite-polarity patches of strong flux. These neutral lines were either canceling, or undergoing both emergence and cancelation concurrently. Sterling et al. (2016) also, however, reported observing several other jets with cool-material outflows, consistent with a minifilament eruption from a neutral line, but for which they did not see an actual, well-formed erupting minifilament.

Sterling et al. (2017) looked at coronal jets from a different active region. Again they found clear EMFs for several jets. But other jets in the active region, in particular those from a specific strong-patch subregion of that active region (called region “R2” in that paper) showed copious jets with cool ejected material, but where a clear, well-formed EMF, could not be detected. All of the jets of Sterling et al. (2017), both those with and those without clear EMFs, occurred along neutral lines undergoing flux cancelation. Sterling et al. (2017) investigated closely several of those jets without clear EMFs, and argued that the minifilament eruption model magnetic setup and dynamics for such jets were the same as in the cases where a clear EMF could be identified (including many non-active-region jets). The two studies Sterling et al. (2016, 2017), therefore, suggest that the active region coronal jets showing cool-material outflows but lacking a clear, well-formed EMF likely form via the minifilament-eruption model, but for some not-yet-understood reason, a well-developed cool-material minifilament did not form in those cases.

Nonetheless, for the jets in which we do not observe an EMF, we cannot rule out the possibility that a different mechanism might operate in some cases, such as the Alfvénic magnetic twist-wave process without a cool minifilament (e.g., Shibata & Uchida 1986; Pariat et al. 2009; Kumar et al. 2018). In addtion, in cases where flux emergence is observed, we cannot rule out that jets may be formed due to the flux-emergence model (Shibata et al. 1992; Yokoyama & Shibata 1995).

Moore et al. (2010) and Moore et al. (2013) found that, when observed in soft X-rays, the spires of jets, roughly speaking, fall into two categories: in one case, the X-ray spires remain narrow (compared to the width of the jet’s base) throughout life of the jet; they called these “standard jets.” In the second case, the X-ray spire broadens during the life of the jet, so that its width becomes comparable to the width of the base; they called these “blowout jets.” In this paper we will again look at a set of polar coronal hole jets in both X-rays and in AIA EUV images. As with the jets of Sterling et al. (2015), the jets of this study have EMFs in at least 20 of 21 jets; most of these, 11, are blowout jets, while four are standard jets, and six are uncertain.

We use these jets to address new points that previously have only been suggested or not considered at all by previous coronal jet studies: (1) We study the behavior of the EMFs in minifilament eruptions that make blowout jets (i.e., jets whose spires become broad when observed in soft X-rays). It had been suggested previously that blowout jets have EMFs that are ejected; that is, have minifilaments that erupt out of the jet-base region and escape along the jet spire into the far corona, or even out into the heliosphere. We will find that this holds for several of the blowout jets of this data set, but we will also learn of a new, modified, alternative behavior for the EMFs in some wide-spire jets that has not been pointed out before, resulting in a modified schematic picture for some wide-spire jets. (2) We examine the behavior of the EMFs that result in the four standard jets of this study. Previously, Sterling et al. (2015) suggested that standard jets (i.e., jets whose spires remain narrow when observed in soft X-rays) have mainly confined EMFs, where the EMFs remain largely trapped in the jet-base region. (Sterling et al. 2015 also alternatively suggested that the narrow spires might result from eruptions that are “ejective but very weak,” where “weak” would mean that the EMF’s eruption is very slow and/or faint.) We will confirm that in our four standard-jet cases the EMFs are mostly confined. (3) We will highlight that the visibility of the EMFs in jets can vary widely in different AIA channels. They can be essentially invisible in some channels, while plainly visible in others. This demonstrates that it is necessary to examine multiple AIA channels before concluding that an EMF might not occur in a particular jet.

Before getting into our new data set, we first clarify some points regarding the history and the meaning of the terms "standard" and "blowout" jet.

2. STANDARD AND BLOWOUT JETS

We begin with a brief explanation for the origin of the terms "standard" and "blowout" in describing jets.

During the time when the emerging flux mechanism was still thought to be the cause of jets, and before the concept of the minifilament eruption model for jets was developed, Moore et al. (2010) and Moore et al. (2013) attempted to explain particular characteristics of jets based on the flux emergence model, and variants of that model. The characteristics in question were based on the appearance of the jets when observed in soft X-rays from XRT. The jets of their studies were restricted to polar coronal hole locations. In addition to the X-ray images, the two studies also used He II 304 Å images, from, respectively, the EUVI instruments on the *STEREO* satellites in Moore et al. (2010), and from AIA in Moore et al. (2013).

In the identification of the two types of jets from the XRT images, Moore et al. (2010, 2013) found that in the narrow-spire (standard) jets the base brightening generally remains localized to the JBP at one side of the jet's base. In the second type of jet (blowout), Moore et al. (2010, 2013) found that the spire starts off narrow, but then grows over much of the life of the jet so that the width of the spire becomes comparable to the size of the base. For these blowout jets, usually the base brightening stops being localized to one part of the base, but instead the entire base evolves to glow with a brightness rivaling that of the JBP. In the two Moore et al. (2010, 2013) studies, approximately one-half of the jets fell into each of the two categories.

Moore et al. (2010, 2013) adopted the "standard" and "blowout" names based on the idea that both jet types were a consequence of the emerging flux model. In the case of the narrow-spire jets, they assumed that the jets were due to the process depicted in drawings in Shibata et al. (1992). The emerging-flux bipole would reconnect with surrounding open coronal field (this would be external reconnection, in the language of Sterling et al. 2015). This external reconnection was argued to reconnect the emerging-loop field with open field lines, with some of the closed emerging-loop field lines becoming reconnected to open field lines by the external reconnection. This reconnection also would both heat the coronal plasma, and eject that heated material vertically along the reconnected open field; this would result in the X-ray-jet spire, with the spire emanating from the location of the external reconnection and flowing out along a narrow column. According to this emerging-flux picture, a second product from that external reconnection would be in the form of a new closed loop below the reconnection site; it was envisioned that this would be the JBP brightening at an edge of the base of the jet. In this case, it was imagined that the emerging bipole remained in tact, making narrow-spire jets when enough oppositely directed field between the emerging bipole and the ambient corona built up for reconnection to ensue. Moore et al. (2010, 2013) envisioned that the narrow-spire jets followed this scenario, and therefore they named these jets standard jets, simply because they envisioned that they followed the standard scenario proposed by Shibata et al. (1992).

For the broad-spire jets, Moore et al. (2010, 2013) envisioned that initially the evolution is the same as in the standard-jet case. But in this case, before, at, or after the initial external reconnections, the emerging bipole itself becomes unstable and erupts outward into the overlying corona. This exploding bipole would erupt outward, and material heated via more widespread external reconnections during the eruption would become the jet's spire. Because the erupting bipole would have an extent comparable to the extent of the pre-eruption bipole that forms the base of the jet, this scenario would explain the broad width of the jet spire in these cases. Moreover, internal reconnections of the legs of the erupting emerged bipole would lead to heating and brightening of the entire base region, explaining the increased extent of the base brightening in these cases. (Again after Sterling et al. 2015, we call these reconnections *internal* reconnections, because they occur internal to the closed bipole.) Because the bipole erupts open in this case, Moore et al. (2010, 2013) called these blowout jets.

Thus, the original concept of "standard jet" and "blowout jet" was based on the idea that jets basically resulted according to the emerging-flux idea. In a variant of the original emerging flux model, Moore et al. (2010, 2013) also allow for the possibility that the bipole had stopped emerging, but that it still created the jet when the emerged bipole undulated or was otherwise disturbed, so that the core of the bipole starts to erupt and/or a burst of external reconnection begins between the bipole and the surrounding ambient coronal field. Thus, in the original idea of Moore et al. (2010, 2013), both standard and blowout jets were a consequence of either an emerging, or an already emerged, magnetic bipole undergoing a sudden episode of fast external reconnection with surrounding coronal field; and the JBP was a consequence of this external reconnection, occurring below the site of the external reconnection.

All of this explanation from Moore et al. (2010, 2013) for the cause of standard and blowout jets, however, was before we realized that many (if not all) jets result from minifilament eruptions from the site of the JBP. Therefore, we had to modify our suggestion of what made the narrow-spire and the wide-spire jets. In Sterling et al. (2015), we therefore argued that both the narrow-spire jets and the wide-spire jets are made by minifilament eruptions. Sterling et al. (2015) further suggested that the difference came about based on whether the EMF was confined to the base, in which case the spire would be narrow (and hence a "standard jet"), or ejected so that it explosively escaped from the base (making a broad-spire "blowout jet"). Thus, the term "standard jet" should be considered a misnomer: that name implies that the narrow-spire jets are formed by the emerging-flux model, which Moore et al. (2010, 2013) had regarded as the standard model for jets. But the evidence supports that those standard jets (and blowout jets too) result from minifilament eruptions, at least for many jets. (Perhaps "narrow-spire jet" and "broad-spire jet" would have been more descriptive names for these types of jets, but the names "standard jet" and "blowout jet" are now historically tied to these respective jet types.)

So in summary: the evidence we have currently is that both X-ray broad-spire jets (named blowout jets), and X-ray narrow-spire jets (named standard jets) result from minifilament eruptions.

One of the topics of our current study is to examine the behaviors of the EMFs in the blowout jets (i.e., our X-ray-observed broad-spire jets) and in standard jets (i.e., our X-ray-observed narrow-spire jets) in our data set. For this set of events, we will examine in closer detail than before the behavior of the EMFs in these jets. Specifically, we will ask whether our blowout jets always have ejective EMFs, and whether the four standard jets of our study have confined EMFs. This is not meant to be comprehensive statistical study of this question, but, using the jets of each type in our set, for the first time we will study the behavior of the EMFs in the jets.

3. INSTRUMENTATION AND DATA

We use data from *Hinode*/XRT and *SDO*/AIA for this study. *Hinode* (Kosugi et al. 2007) was launched in 2006, and observes the Sun from Earth orbit. XRT (Golub et al. 2007) observes the Sun in soft X-rays, over a range spanning a few Å to ∼100 Å, using a variety of filters. For this study we restrict our observations to those taken with the "Al Poly" filter, as it is sensitive to relatively cool temperatures in the range of $\sim 10^6$ K (Narukage et al. 2014). These images are appropriate for observing X-ray jets in polar coronal holes, which often have spire temperatures in the ∼1—2 MK range (Pucci et al. 2013; Paraschiv et al. 2015). XRT is capable of observing the Sun with various parameters. For our observations, XRT typically used 60 s or slightly faster cadence, with $1''$ pixels and a field of view (FOV) of $384'' \times 384''$.

SDO/AIA observes the Sun with seven EUV filters, identified by the wavelengths 304, 171, 193, 211, 131, 94, and 335 Å, listed in roughly ascending order from lower to higher temperature sensitivity for non-flaring plasmas, covering $\sim 10^5$—10^7 K (Lemen et al. 2012). Sterling et al. (2015) concluded that the hottest three channels: 131, 94, and 335 Å, added little to the investigation of the processes driving the jets observed in polar coronal holes. Therefore for this study we only include the first four channels in our data. AIA observes the entire solar disk with 12 s cadence in these filters, with pixels of $0.''6$.

Our observed jets can sometimes have weak signal in our selected passbands. For the work here we have increased the signal by summing two consecutive images for both our XRT and AIA images. We formed the presented accompanying videos as running sums of the images, maintaining the 12 s cadence for the AIA movies and about 1 min cadence for the XRT movies. Additionally, we have enhanced visibility of faint features by taking the fourth root of the intensities, and we present the resulting images and videos with a typical logarithmic scaling.

We selected the jets for our study from the XRT images rather than from AIA. The reason for this is two fold. First: We are interested specifically in observing X-ray jets, because that is what was used to identify standard and blowout jets in the Moore et al. (2010, 2013) studies. But jets that stand out in EUV wavelengths may not necessary be prominent, or even visible at all, in X-rays. Thus, to be certain that we are observing X-ray jets, it is necessary to start with the X-ray images. Second: Because the XRT data are not of the full-disk synoptic form of AIA, first selecting jets with AIA would not guarantee that XRT was observing the region of interest at the same time. But AIA data are almost certainly available for any of the selected XRT time periods, provided that the data are from after AIA started operations in 2010; thus any of the jets we select from XRT images after that time will almost certainly have corresponding AIA images.

We selected time periods when *Hinode* was running the *Hinode operations program* (HOP) 81, which has been regularly done by the *Hinode* team beginning early in the mission. This HOP observes the polar coronal hole regions, with XRT typically taking observations in selected filters for several consecutive hours. We looked for data during 2017 and 2018, when the polar coronal holes were present again following the maximum of solar cycle 24. For ease of analysis, we searched for periods of continuous observations over several hours in which it was obvious from low-resolution quick-look data that several jets would be included. Our aim was not to do a completely random statistical study of all jets, but rather we were looking for a sizable number of clear X-ray jets to investigate together with AIA data. We settled on data sets from four dates: 2017 January 13, 2017 March 6, 2017 July 4, and 2018 April 3. Our resulting data set includes 21 jets in polar coronal holes that were well observed by XRT; as expected, AIA data are available for all of these events. Due to the near-pole location of these jets, we did not attempt to analyze corresponding magnetic field data, as the signal for such near-limb non-active-region locations is usually too weak to be useful.

Table 1 lists our selected jets, which we have labeled chronologically as J1—J21. Figures 1, 2, 3, and 4 show XRT snapshots for the four time periods, with some of the jets labeled. Accompanying animations show the complete periods of observation, with all of the jets labeled. As can be ascertained from the videos, we selected only a selection of all the jets visible in each animation. We selected most of the obvious strong jets, but for various reasons omitted some jets that were prominent in XRT. One such reason is that some jets very near the limb did not seem appropriate for analysis after a cursory inspection of the corresponding AIA images. For example, the jet in Figure 4 west of Jet J18, near coordinates (0,950), is prominent in XRT. When we looked at the corresponding AIA images however, we were not confident that we were able to observe adequately the near-photosphere dynamic activity leading to the jet, and therefore we did not include that jet in our study. Another reason for why we omitted some otherwise-attractive XRT jets was because of a gap in the continuity of one of the data sets. While most of the selected jets stand out in XRT images, for variety we have included a few jets that are less prominent yet still distinct in XRT; jets J7, J8, J12, and J19 being such jets.

Columns two and three of Table 1 give the date and time of the start of each jet, and column four gives the jet duration. One has to make a choice in deciding when a jet starts. We have opted to use as the start time the XRT frame in the videos accompanying Figures 1—4 that first shows the spire of the jet starting to grow. This too can be somewhat subjective, and thus there is an uncertainty in the start time of approximately one frame of the XRT movies. Similarly, we define the duration based on when the spire is no longer visible. Another equally acceptable option for defining duration would have been to use the time that the base starts to brighten as the jet start time; doing so would increase the estimated duration over that obtained via our adopted method by several minutes in some cases.

Column 4 of Table 1 gives our assessment of each jet as standard, blowout, or uncertain, based on the width of its spire in the XRT images. We will discuss these aspects of the jets in §6. Before that however we will consider the activity at the base of the jets in §§4 and 5.

4. ERUPTING MINIFILAMENT BEHAVIOR AT JET BASES

4.1. *Over-and-Out Erupting Minifilaments*

We have found that the appearance of the EMF is different in different jets. One variety are what can be called “over-and-out” EMFs. They basically fit the picture of Sterling et al. (2015), where the minifilament starts at one side of the large lobe, and migrates over to near the top of that lobe, and then largely escapes through newly opened field there. These eruptions are similar to a larger class of over-and-out eruptions, ranging from jet features to CMEs (e.g. Bemporad et al. 2005; Moore & Sterling 2007; Sterling et al. 2011; Gopalswamy et al. 2014; Panesar et al. 2016a; Yang et al. 2018).

We show two examples from this over-and-out EMF category. Figure 5 shows the first of these examples, which is event J11 of Table 1. This EMF is visible in all four of our AIA channels. We display our example jets in four-panel image arrays, where panels (a), (b), (c), and (d) respectively show the same FOV in the AIA 171, 193, 211, and 304 Å channels, at approximately the same time. Panels (e), (f), (g), and (h) show the same for a different time period. The corresponding video shows the same images over the duration of the event. Panel (i) and the corresponding video show the jet in XRT images (with a different FOV from the (a)-(h) AIA images). Early movement of the minifilament (blue arrows in Fig. 5) becomes obvious from about 13:07 UT (see the corresponding video). The feature travels toward the southwest from then until about 13:18 UT, when its trajectory changes to a more southerly direction, and then travels in that direction outward along the jet’s spire (green arrows). In this case, pre-jet ambient open field lines along the line of sight to the newly reconnected open field lines upon which the spire forms apparently already contain material prior to the event, so that they form a plume-like structure visible in the the 171, 193, and 211 Å channels in the (a)—(d) panels. An enhancement flows out along the western edge of the structure at the time of the right-side panels in the figure and accompanying video, forming the spire. In XRT (animations in Figs. 2 and 5), this jet is comparatively weak; its JBP is likely faintly visible in the frames at 13:15 and 13:16 UT, although it is more apparent in the AIA images (red arrow in Fig. 5 points to it). From those AIA images, and also from the XRT videos as the spire becomes more visible, at about 13:23 UT for example, it is apparent that the JBP occurs on the northeast side of the spire. This is consistent with the JBP forming at the location from where the minifilament erupted in the AIA images, consistent with Sterling et al. (2015). The brightening of the large lobe from the external reconnection (straddling M1—M2 in Sterling et al. 2018; also see Fig. 9, below) is apparent in XRT images from about 13:18 UT, and from about 13:20 UT in the AIA images (yellow arrows). In this case, this lobe outshines the JBP, consistent with a common occurrence in blowout jets reported by Moore et al. (2010, 2013).

In Figure 6, Jet J18 shows another example of this type of jet-producing minifilament eruption, this time viewing the phenomenon in profile (side-on). In this case, our perspective is looking from the left side of the schematic of Sterling et al. (2015), from a low angle above the photospheric level. From the animation accompanying the figure, a minifilament (or at least one component of a minifilament) initially resides on the far side of the large lobe (the lobe between M1 and M2 in Fig. 9). As it starts erupting, this minifilament closely hugs the curve of the M1—M2 lobe, as in the four left-hand panels of Figure 6. That video also shows a JBP brightening at about 14:55 UT. Some minutes later in the right-hand panel, at about 15:15 UT, much of this minifilament is erupting outward. Green arrows in Figure 6 show the cool-component strands of that EMF. Prior to that time, from about 14:58 UT until at least 15:08 UT, there are brightenings visible in the 171, 193, and 211 Å channels corresponding to the hot spire, *sans* the cool material; in the corresponding XRT movie, a bright X-ray spire is visible over about 14:51—15:08 UT, and these hot-spire observations correspond to the middle panel (panel b) of the schematic in Sterling et al. (2015). Thus, all of the key aspects of the Sterling et al. (2015) schematic are apparent in this jet. (This description however may be oversimplified somewhat, as another minifilament component, in the foreground of the component of the minifilament just discussed, is apparently undergoing eruption between 14:49 and 14:59 UT. Due to the single viewing perspective, it is not possible to sort out the detailed connection between these different minifilament components.)

There are several other examples of the same basic type of eruption in our data set. For example, jets J4, J13, and J14 all apparently belong to this category of over-and-out EMF. Each of these cases show well the minifilament corresponding to times between the those represented by the first two panels (panels (a) and (b)) of the Sterling et al. (2015) schematic.

4.2. *Largely Confined Erupting Minifilaments*

A second type of EMF that we observed in our data set is one where the in-motion minifilament appears to be confined very low near the surface, as it travels on top of the magnetic lobe between locations M1 and M2 in Figure 9(a). In many cases it can appear to execute a revolving type of motion as it travels over the top of that lobe in a direction away from its ejection location. In our data set, jets J5, J16, J18, J20, and probably J17, exhibit this type of behavior. Here we present two examples; we present jet J5 because it shows the phenomenon well, and we present J20 because it gives key insight into what is occurring. We are forced to say that these are "largely confined," because frequently we cannot confirm that all of the cool minifilament material remains fully confined; some of it may "leak out" along opening field lines, or in some cases it might be ejected directly toward us (and hence hard to observe) later in its evolution. But at least for much of the duration of these minifilament eruptions, a substantial portion of the cool material appears to be confined near the solar surface.

Figure 7 shows the same four AIA channels as in the previous examples, this time for jet J5 of Table 1. As is apparent from the accompanying video, in this case the minifilament starts erupting at about 11:01 UT from about y location -770. An absorbing clump of it is visible passing over the location of Figure 7(a—d) around 11:03 UT, and then seems to settle on the NE side of the frame near the end of the video at 11:30 UT. Thus, it seems as if the minifilament revolves around an axis in the plane of the image that runs along a SE-NW diagonal in the frame. From 211 Å panel (Fig. 7(c), and also but less apparent in Fig. 7(d)), the spire of the jet emanates from that revolving EMF; this is what causes the broad spire in the corresponding XRT video. This apparently corresponds to the case of the schematic in Sterling et al. (2015), but where the minifilament travels beyond the apex of the large lobe field. The corresponding large lobe is faintly apparent in AIA 211 Å images (yellow arrow in Fig. 7(c)), although it is much more apparent in the XRT video over about 10:57—11:09 UT. In this case, only a hot spire is visible. At least up until this time (11:09 UT), little if any of the cool minifilament material appears to have been ejected outward in this case. After this time it is hard to discern the minifilament's status; much of it might have been thrown to the far side of the large-lobe field, or alternatively much of it may have encountered, reconnected with, and escaped along open field directed toward the observer (making that ejection hard to discern), in which case it would, eventually, be of the over-and-out variety. We can say that the X-ray spire is prominent between about 11:00 UT and 11:23 UT, and so its earliest (and strongest expansion) phase occurred when much of the EMF was still confined to a comparatively low altitude.

Our second example in this category, shown in Figure 8, also displays a rolling (revolving) type motion. This jet, jet J20 of Table 1, occurs at the same location as jet J18, occurring about 100 min following that earlier jet (Jet J18 is in Fig. 6 and corresponding video, and Jet J20 is in Fig. 8 and corresponding video); thus jets J18 and J20 might be called homologous, although close inspection does reveal some differences. In jet J20, as with jet J18, a minifilament erupts on the far side of the M1—M2 (larger) magnetic lobe of the Sterling et al. (2015) schematic. It reaches the apex of the lobe near the time of Figure 8(a—d). Unlike jet J18 however, very little of the cool minifilament material obviously erupts outward; compare the frames in the video in Figure 6 near 15:14 UT, with those of the video of Figure 8 near 16:43 UT; relatively little of the cool material is erupting outward in the jet J20 case, compared to jet J18. On the other hand, more of the cool material continues moving to the near side of the magnetic lobe than in the jet J18 case, with the blue arrows of Figure 8(e) showing prominent clumps of material on the near side of that lobe. Similar features can be seen in the jet J18 video, but they are much less apparent. Thus apparently more of the minifilament was ejected in the jet J18 case compared to the jet J20 case.

We believe that jets J20 (Fig. 8) and J5 (Fig. 7, at least for much of its life) are showing similar behavior of EMFs, but from differing perspectives. Figure 9 depicts a schematic corresponding to that of Sterling et al. (2015), showing these cases where the EMF is mostly confined to the base region. In this case, the minifilament eruption proceeds as in the Sterling et al. (2015) schematic through panel (b), which is Figure 9 panel (a). Then however, the external open field encountered at the apex of the M1—M2 magnetic lobe does not impede fully the movement of the minifilament flux rope from right to left in the figure. It continues to move onto the far side of the lobe. As it does so, the magnetic field surrounding the minifilament/flux rope continues to reconnect with the ambient coronal field. This produces a hot spire occurring progressively further from the eruption site and the JBP. A cool spire however (expected to be visible in AIA 304 Å images) would be minimal or absent, as long as the external reconnection does not eat far enough into the minifilament flux rope's core region.

In addition to events J5 and J20, other jets in our table have partially confined EMFs. The EMF in jet J16 is also clearly of this revolving type; it is seen from a perspective similar to that of jet J5. Jet J17 has an EMF that is somewhat harder to see than the others. It seems to be similar to these others, but the EMF appears to make it only partially past the apex of its M1—M2 lobe. Thus, in general, these revolving type of EMFs follow the schematic picture of Figure 9.

Jet J15, displayed in Figure 10 and in the accompanying video, also perhaps has a confined EMF. Over about 12:49—13:02 UT, the minifilament appears to be erupting nearly radially from the surface. Then, between about 13:02—13:12 UT, it moves first laterally toward the east, and then downward also, appearing to return to the surface. This is what is more commonly regarded as a confined filament eruption, whereby the eruption leaves the base region but then is aborted, presumably by overlying strong-enough magnetic field (e.g. Moore et al. 2001; Ji et al. 2003; Sterling et al. 2011). Thus in this case, the confined eruption basically follows the schematic of Sterling et al. (2015), but where the erupting cool minifilament material, along with much of the magnetic flux rope surrounding and accompanying that cool material, has its outward eruption impeded by overlying stronger field shortly after the situation depicted in panel (c) of Sterling et al. (2015). If viewed from a different perspective (looking "down from above"), this minifilament might also appear to be undergoing a revolving-type motion.

5. ERUPTING MINIFILAMENT CHARACTERISTICS

5.1. *Erupting-Minifilament Physical Characteristics*

We have measured the lengths (projected on the plane of the sky) of the EMFs for each of the events, with the results presented in Table 1. There are several considerations in these measurements: the EMFs are sometimes difficult to discern, and we cannot always measure them at the same stage in their eruption (e.g., some are visible at low altitudes, while others are obscured by foreground material at low altitudes). Also, they change shape during the course of their eruption, and the EMFs for different jets are not consistently visible in the same AIA wavelengths (see below). Despite these issues, the features we observe are essentially always features showing in absorption in the 171, 193, and/or 211 EUV channels (304 can have a strong emission component), and therefore we expect that we are seeing a substantial portion of the cool-material minifilament in each case. In other words, we expect that we are observing and measuring features representative of the erupting cool-material minifilament for each case. Given these and other factors however, our values should be considered as estimates good to within about a few tens of percent. With these caveats, the average values and standard deviations for our measured EMF lengths are $14'' \pm 7''$. The comments column of Table 1 gives the specific AIA channel used for the measurement for each case.

We also estimated velocities of the EMFs, by estimating the distance traveled by the structure over a selected time range where we could track the feature with fair confidence. Again there are various uncertainties that were unavoidable. Perhaps the biggest was that we could not consistently observe the erupting feature reliably during the same stage of eruption for differing events. For example, from on-disk observations, we have determined that the EMFs frequently start their eruption with a relatively slow rise, and later undergo an acceleration to a faster speed (Panesar et al. 2020), similar to what is frequently observed in erupting large-scale filaments (e.g., Tandberg-Hanssen et al. 1980; Sterling & Moore 2003; Sterling et al. 2007; Imada et al. 2014; McCauley et al. 2015; Cheng et al. 2020). For our near-limb observations here however, it can be difficult to discern whether a moving minifilament is in its slow-rise or fast-rise phase, because the initiation of its rise is sometimes hidden from view by foreground chromospheric obscuring material. Also, the inability to determine reliably the orientation of the EMF with the line of sight makes speed determinations more complex. (On the other hand, the near-limb perspective allows for a better estimate of the radial velocity, based on visual displacement over time, of the EMF than do the on-disk measurement, since the latter will have a larger component of the radial velocity directed along the line of sight) Therefore, we again can only present our measurements as an estimate of the rise speeds of the X-ray-jet-producing EMFs during the early stages of their eruption. From all of the results given in Table 1, we find the average value and standard deviation of the speeds to be $26 \pm 13\,\mathrm{km\ s^{-1}}$. For each jet, we estimated the speeds using the same AIA channel as we used for measuring the EMF's size.

We have also measured the duration times for the jets, using the XRT images. This was most straight forward, because these images were used for the original identification of the jets. Moreover, the visibility of the jet spires in the AIA images varied, with some jets showing little or no spire in some of the AIA channels, despite having an obvious spire in XRT. We used as the duration the time over which the spire was discernible in the accompanying XRT videos (Figs. 1—4). Usually some base brightening preceded the spire's appearance, and also sometimes brightening happened after the spire's disappearance; we ignored these base brightenings in these duration estimates. We estimate that there is an uncertainty of approximately one minute in the durations given in Table 1. From those values, we obtain an average duration and standard deviation of $21 \pm 10\,\mathrm{min}$ for our 21 events.

5.2. *Erupting-Minifilament Visibility*

We can make an assessment of how readily visible the EMFs are for our 21 events. Because this is a visual assessment, there necessarily is a subjective element to this exercise. Moreover, the assessment also depends upon the manner in which the data are examined; we have described our display methods for the movies we use earlier: a running sum over two consecutive images, and displayed on a logarithmic scale after taking the fourth root of the intensities. We do not believe however that our assessment of whether an EMF was visible would have changed substantially with a standard scaling of unsummed AIA images, on a logarithmic scale but no further enhancements. Most important was to zoom into the eruption region close enough, and to adjust the scaling maximum and minimum range values appropriately. With the realization however that the EMFs might be confined to the base region of the jet and possibly with little or no obvious outward ejection into the corona, as with several examples in §4.2, and as depicted in Figure 9, then the identification can become more apparent for some cases with the zoom-ins and maximum/minimum intensity scalings.

Of the 21 events, we assess that 11 of the X-ray jets have relatively easily identifiable EMFs. These are event numbers J2, J4, J5, J11, J13, J14, J15, J16, J18, J20, and J21. Several of these are displayed as examples in §4.

We assess that six events have EMFs that are medium difficult to identify: J1, J6, J8, J9, J17, J19. We assess that in three events an EMF is detectable but difficult to identify: J3, J7, J10.

In one event in particular, J12, it is difficult to identify unambiguously an EMF. That event, however, is consistent with being driven by a minifilament-eruption type of eruption. This event is very small, with a base size of $\sim 15''$, which complicates possible EMF detection. Moreover, the location of that jet's origin seems to be substantially obscured by absorbing foreground structures, due to the jet's near-limb location. Activity that we see in AIA at the jet's base appears to be consistent with a minifilament-eruption type of eruption. Moreover, we can identify a candidate for an EMF, especially in 211 Å, over 14:03—14:05 UT, but the evidence is less compelling than the other jets of this particular data set. Thus we can say that we lack clear visual evidence of an EMF in this case.

We do not know how the events having hard-to-see EMFs operate. If they do operate essentially the same as depicted in the schematics of Sterling et al. (2015) and Figure 9, then EMFs might be hard to discern due to the events' small size and/or the diffuse coronal background. Their sizes are comparatively small; for example, we estimated the sizes of J6, J7, J8, and J9 as $\lesssim 10''$, and so substantially below the average value of $14''$. In some cases they are very diffuse and ill-defined, as with jet J19, and also jet J1; in these cases what we see as a potential EMFs appear loosely consolidated, akin to the very large filament observed by *Hinode* by Berger et al. (2011), and it makes it hard to determine with certainty whether the J1 minifilament was actually ejective or mainly confined (hence we say its ejection is "uncertain"). We also find that foreground "coronal haze," resulting from either the jet occurring inside of the quiet Sun, or due to quiet Sun corona being positioned in front of the jet along the line of sight, can make it substantially more difficult to observe EMFs and jet spires, if they exist in these cases.

At other times, the EMFs appear to be present, but intrinsically faint. Figure 11 shows an example of this in jet J3, where a likely EMF is faintly visible rising from about 12:50 UT to 13:04 UT, and then expanding outward as the jet spire forms over the next several minutes. It is unclear whether this EMF is confined or ejective. In 171 it appears as if part of it may be ejecting outward over about 13:10—13:20 UT, but there is not a clear corresponding feature visible in the other three AIA channels. Thus we cannot determine whether the minifilament truly ejects but this is only apparent in 171, or if the apparent 171 feature is darkening due to field opening or some other factor. All four AIA channels do however show some eruptive minifilament activity corresponding to the X-ray jet, but it is unclear whether that EMF is ejective or confined in this cases.

6. STANDARD (NARROW) AND BLOWOUT (WIDE) JETS IN THE SET

We made an assessment of whether jets were standard or blowout based solely on the appearance of their spires as wide or narrow in XRT images, which was a key assessment consideration used by Moore et al. (2010, 2013). We call the XRT-narrow-spire jets "standard" the XRT-wide-spire jets "blowout," and ambiguous and/or uncertain jets we labeled as "uncertain." Column 5 of Table 1 gives these assessments for each of our events. We identify 11 jets as blowout, four as standard, and six as uncertain.

Table 2 groups the jets based on the type: blowout, standard, or uncertain. Of the eleven blowout jets, only three came from clearly ejective minifilament eruptions. Two of them appear to be from mainly confined eruptions, and another five are from either partially confined eruptions or from eruptions that were uncertain regarding whether the cool minifilament material was ejected outward along the spire's open coronal field.

The four jets that we classify as standard, on the other hand, all originate from eruptions of minifilaments that are either confined, partially confined, or uncertain. That is, no clearly ejective EMF occurred in the four standard jets, which, however, is a small sample of cases.

The jets that were classified as "uncertain" regarding being standard or blowout had various spire appearances, as described in the table. These uncertain cases included both confined and ejective minifilament eruptions.

7. SUMMARY AND DISCUSSION

We selected 21 X-ray solar polar coronal jets using *Hinode*/XRT images, and examined their origin using *SDO*/AIA images. Essentially all of these events show evidence for originating from the eruption of minifilaments, consistent with the findings of Sterling et al. (2015). The ease of detecting the EMF varied.

Our set included 11 so-called blowout jets, if defined as jets whose spires grow to be wide (comparable in size to the size of the jet's base) when viewed in XRT images. We found that these blowout jets can have EMFs that appear to be ejected or confined, or where the eruption type is more ambiguous. Thus it is not only ejective EMFs that occur in blowout jets, as previously speculated (e.g. Sterling et al. 2015). Our selection of 21 events only included four so-called standard jets, where the spire remains narrow (compared to the jet's base) in XRT images. None of these four cases had EMFs that were clearly ejected, but instead were confined, partially confined, or the nature of the minifilament eruption was uncertain. This sample may be too small to conclude that clearly ejective minifilament eruptions never make standard (narrow-spire) X-ray jets.

For the confined-eruption case, we have shown clear cases where much of the minifilament travels a substantial distance more-or-less horizontal to the solar surface, as depicted schematically in Figure 9, rather then becoming trapped near the apex of the base structure.

We can offer some speculations about why a largely confined minifilament eruption can still produce a broad-X-ray-spire "blowout" jet. One possibility is that the envelope surrounding the confined cool minifilament undergoes extensive external reconnection with open field as the minifilament-carrying flux rope is traveling across the large base lobe, basically as depicted in Figure 9, where the reconnections persist more-or-less continuously as the EMF traverses the lobe from M2 to M1. This could occur, e.g, in a 3D situation whereby part of the EMF-carrying flux rope extends back toward the JBP, so that the external reconnections continuously occur from the leading edge of the EMF back to the JBP, making a broad curtain-like spire. This would therefore appear as a (broad-spire) blowout jet. When the EMF does not have continuous extensions backward toward the JBP, then it could be that only a short leading edge of the EMF undergoes external reconnection, forming a (narrow-spire) standard jet. Another possibility for a confined EMF to occur with a (broad-spire) blowout jet is that there could be a flux rope without cool material situated above the cool-material minifilament-carrying flux rope represented by the blue circle in Figure 9. That higher-altitude flux rope would be essentially invisible in our X-ray and EUV images, but it could be destabilized by the eruption of the cool-material-carrying minifilament flux rope, and undergo an ejective eruption that makes the broad-spire jet. This would be similar to the "lid-removal"-type mechanism occurring in some large-scale filament eruptions (Török et al. 2011; Lynch & Edmondson 2013; Sterling et al. 2014), as in double-decker (or multiple-decker) filament eruptions whereby one or more filaments stacked at different heights above the same neutral line sequentially erupt (e.g. Su et al. 2011; Joshi et al. 2020). Which mechanism is acting perhaps could be a factor in whether the spire resulting from the confined minifilament eruption becomes wide, as depicted in Figure 9, thus forming a blowout jet, or remains narrow, thus forming a standard jet. Details of whether these specific mechanisms are operational in our events is beyond the scope of the present study.

Of the 21 the events, for 11 of them, or about 50%, we assess that the identification of the EMFs was relatively easy, using standard high-cadence AIA videos focused in on the jet-base region (usually with a FOV of $100'' \times 100''$ or smaller). In nine of the remaining cases, about 40%, we saw evidence for minifilament eruptions that we classified as medium-difficult or difficult to identify. These non-easy cases were jets where we were still confident that a minifilament eruption was occurring, but which are more difficult to make out visually. In only one case were we not confident of discerning at least a faint EMF.

Regarding visibility of EMFs in different AIA channels, corresponding to X-ray jets: In some cases, the EMFs accompanying our X-ray jets were visible in as few as one of the four EUV channels we examined, and frequently they were not equally apparent in all four channels. Therefore it is critical to examine multiple EUV wavelengths before concluding that any given jet may not have an EMF at its base. This is similar to the situation with X-ray jet observations prior to availability of high-cadence EUV images: EMFs are essentially invisible in soft X-rays; to see them, one must also inspect concurrent EUV images. Here we have learned that one cannot always rely on a single EUV wavelength channel for a complete search of the EMFs that might occur at the base of a given X-ray-observed jet.

The lengths of the EMFs are $14'' \pm 7''$. This is not far different from the values of $11'' \pm 7''$ found by Sterling et al. (2015), who also looked at minifilaments that produced polar coronal hole XRT jets. These values are somewhat smaller than the $\sim 25''$ average minifilament size, and $\sim 23''$ for jet-base widths, reported for ten quiet-Sun jets by Panesar et al. (2016b). That Panesar et al. (2016b) study, however, estimated the full (curved) length of the minifilament viewed on disk prior to its eruption; we instead measure the length of the minifilaments at the start of or just after eruption onset, and we measure the projected length against the plane of sky, without attempting to estimate the full length along the axis of the minifilament. Another difference is that the Panesar et al. (2016b) jets were selected from full-disk AIA images, while we used XRT images focused in on a smaller FOV; it is unclear how jets selected from AIA compare with those selected via our procedure. Panesar et al. (2018) measured the base size of 13 AIA-observed on-disk coronal hole jets, and found values of $16'' \pm 8''$, where they used the methods of Panesar et al. (2016b) to find the base size of those coronal-hole jets. (One might assume that, similar to what was found in Panesar et al. 2016b, the lengths of the minifilaments of Panesar et al. 2018 pre-eruption minifilaments are probably similar to the size of the jet-base region.)

We found speeds of the EMF, when they were in the process of erupting, to be $26 \pm 13\,\mathrm{km\ s^{-1}}$. This is substantially faster than the values near $1\,\mathrm{km\ s^{-1}}$ reported by Panesar et al. (2020) from the earliest stages of the onset of their minifilament eruptions. Here we are likely favoring speeds of the minifilaments in their fast-rise phase, while those of Panesar et al. (2020) are favoring the slow-rise stages. There may also be a difference due to the above-mentioned viewing perspective, with our observations here showing the rising minifilaments in profile (so that radial outward motions would show as a displacement in the plane of the sky),while the Panesar et al. (2020) study would, on average, have a larger component of the radial velocity along the line of sight. Thus the Panesar et al. (2020) investigation may have systematically measured somewhat lower velocities than our study.

Kumar et al. (2019) examined 27 on-disk coronal-hole jets using AIA 304, 171, and 193 Å images, and report that 67% "are associated with" minifilament ejections/eruptions. They also report that the remaining events also displayed evidence for an eruption of a filament channel without cool material. These findings are in general agreement with what we find here, and in the studies referenced in the preceding paragraphs. Nonetheless, in light of our results presented here (and also discussed in Sterling et al. 2015), we wonder whether some of those remaining 33% in the Kumar et al. (2019) study might have EMFs that erupted in the manner described in Figure 9, and thus were not recognized as minifilament eruptions in that study because of the lack of a clear minifilament ejection into the higher corona.

The authors received funding from the Heliophysics Division of NASA's Science Mission Directorate through the Heliophysics Guest Investigators (HGI) Program, and the MSFC *Hinode* Project. *Hinode* is a Japanese mission developed and launched by ISAS/JAXA, with NAOJ as domestic partner and NASA and UKSA as international partners. It is operated by these agencies in co-operation with ESA and NSC (Norway). We acknowledge the use of AIA data. AIA is an instrument onboard *SDO*, a mission of NASA's Living With a Star program.

REFERENCES

Adams, M., Sterling, A. C., Moore, R. L., & Gary, G. A. 2014, Astrophysical Journal, 783, 11, doi: 10.1088/0004-637X/783/1/11

Bemporad, A., Sterling, A. C., Moore, R. L., & Poletto, G. 2005, Astrophysical Journal, 635L, 189, doi: 10.1086/499625

Berger, T., Testa, P., Hillier, A., et al. 2011, Nature, 472, 197, doi: 10.1038/nature09925

Chen, P. F. 2011, Living Reviews in Solar Physics, 8, 1, doi: 10.12942/lrsp-2011-1

Cheng, X., Zhang, J., Kliem, B., et al. 2020, ApJ, 894, 85, doi: 10.3847/1538-4357/ab886a

Cheung, M. C. M., De Pontieu, B., Tarbell, T. D., et al. 2015, ApJ, 801, 83, doi: 10.1088/0004-637X/801/2/83

Cirtain, J. W., Golub, L., Lundquist, L., et al. 2007, Science, 318, 1580, doi: 10.1126/science.1147050

Doyle, L., Wyper, P. F., Scullion, E., et al. 2019, ApJ, 887, 246, doi: 10.3847/1538-4357/ab5d39

Fang, F., Fan, Y., & McIntosh, S. W. 2014, Astrophysical Journal, 789, 19, doi: 10.1088/2041-8205/789/1/L19

Golub, L., Deluca, E., Austin, G., et al. 2007, Solar Physics, 243, 63, doi: 10.1007/s11207-007-0182-1

Gopalswamy, N., Xie, H., Akiyama, S., Mäkelä, P. A., & Yashiro, S. 2014, Earth, Planets, and Space, 66, 104, doi: 10.1186/1880-5981-66-104

Hinode Review Team, Khalid, A.-J., Patrick, A., et al. 2019, Publications of the Astronomical Society of Japan, 71, id.R1, doi: 10.1093/pasj/psz084

Hirayama, T. 1974, Solar Physics, 34, 323, doi: 10.1007/BF00153671

Hong, J., Jiang, Y., Yang, J., et al. 2014, Astrophysical Journal, 796, 73, doi: 10.1088/0004-637X/796/2/73

Hong, J., Jiang, Y., Zheng, R., et al. 2011, Astrophysical Journal, 738L, 20, doi: 10.1088/2041-8205/738/2/L20

Huang, Z., M., S., M., Doyle, J. G., & Lamb, D. A. 2012, Astronomy and Astrophysics, 548, 62, doi: 10.1051/0004-6361/201220079

Imada, S., Bamba, Y., & Kusano, K. 2014, PASJ, 66, S17, doi: 10.1093/pasj/psu092

Innes, D. E., Bučík, R., Guo, L. J., & Nitta, N. 2016, Astronomische Nachrichten, 337, 1024, doi: 10.1002/asna.201612428

Ji, H., Wang, H., Schmahl, E. J., Moon, Y.-j., & Jiang, Y. 2003, Astrophysical Journal, 595L, 135, doi: 10.1086/378178

Joshi, N. C., Sterling, A. C., Moore, R. L., & Joshi, B. 2020, ApJ, 901, 38, doi: 10.3847/1538-4357/abacd0

Joshi, R., Schmieder, B., Chandra, R., et al. 2017, SoPh, 292, 152, doi: 10.1007/s11207-017-1176-2

Kosugi, T., Matsuzaki, K., Sakao, T., et al. 2007, Solar Physics, 243, 3, doi: 10.1007/s11207-007-9014-6

Kumar, P., Karpen, J. T., Antiochos, S. K., et al. 2018, Astrophysical Journal, 854, 155, doi: 10.3847/1538-4357/aaab4f

—. 2019, Astrophysical Journal, 873, 93, doi: 10.3847/1538-4357/ab04af

Lemen, J. R., Title, A. M., Akin, D. J., et al. 2012, Solar Physics, 275, 17, doi: 10.1007/s11207-011-9776-8

Lynch, B. J., & Edmondson, J. K. 2013, ApJ, 764, 87, doi: 10.1088/0004-637X/764/1/87

McCauley, P. I., Su, Y. N., Schanche, N., et al. 2015, SoPh, 290, 1703, doi: 10.1007/s11207-015-0699-7

McGlasson, R. A., Panesar, N. K., Sterling, A. C., & Moore, R. L. 2019, ApJ, 882, 16, doi: 10.3847/1538-4357/ab2fe3

Moore, R. L., Cirtain, J. W., Sterling, A. C., & Falconer, D. A. 2010, Astrophysical Journal, 720, 757, doi: 10.1088/0004-637X/720/1/757

Moore, R. L., & Sterling, A. C. 2007, ApJ, 661, 543, doi: 10.1086/516620

Moore, R. L., Sterling, A. C., Falconer, D. A., & Robe, D. 2013, Astrophysical Journal, 769, 134, doi: 10.1088/0004-637X/769/2/134

Moore, R. L., Sterling, A. C., Hudson, H. S., & Lemen, J. R. 2001, Astrophysical Journal, 552, 833, doi: 10.1086/320559

Moreno-Insertis, F., & Galsgaard, K. 2013, Astrophysical Journal, 771, 20, doi: 10.1088/0004-637X/771/1/20

Muglach, K. 2021, ApJ, 909, 133, doi: 10.3847/1538-4357/abd5ad

Mulay, S. M., Matthews, S., Hasegawa, T., et al. 2018, SoPh, 293, 160, doi: 10.1007/s11207-018-1376-4

Mulay, S. M., Tripathi, D. T., Del Zanna, G., & Mason, H. 2016, Astronomy and Astrophysics, 589, A79, doi: 10.1051/0004-6361/201527473

Narukage, N., Sakao, T., Kano, R., et al. 2014, SoPh, 289, 1029, doi: 10.1007/s11207-013-0368-7

Nishizuka, N., Shimizu, M., Nakamura, T., et al. 2008, Astrophysical Journal, 683, 83, doi: 10.1086/591445

Nisticò, G., Bothmer, V., Patsourakos, S., & Zimbardo, G. 2009, Solar Physics, 259, 87, doi: 10.1007/s11207-009-9424-8

Panesar, N. K., Moore, R. L., & Sterling, A. C. 2020, ApJ, 894, 104, doi: 10.3847/1538-4357/ab88ce

Panesar, N. K., Sterling, A. C., & Moore, R. L. 2016a, Astrophysical Journal, 822L, 7, doi: 10.3847/2041-8205/822/2/L23

—. 2017, Astrophysical Journal, 844, 131, doi: 10.3847/1538-4357/aa7b77

—. 2018, Astrophysical Journal, 853, 189, doi: 10.3847/1538-4357/aaa3e9

Panesar, N. K., Sterling, A. C., Moore, R. L., & Chakrapani, P. 2016b, Astrophysical Journal, 832L, 7, doi: 10.3847/2041-8205/832/1/L7

Paraschiv, A. R., Bemporad, A., & Sterling, A. C. 2015, A statistical study with Hinode XRT data, Astronomy and Astrophysics, 579, 96, doi: 10.1051/0004-6361/201525671

Pariat, E. A., K., S., & DeVore, C. R. 2009, Astrophysical Journal, 691, 61, doi: 10.1088/0004-637X/691/1/61

Pucci, S., Poletto, G., Sterling, A. C., & Romoli, M. 2013, Astrophysical Journal, 776, 16, doi: 10.1088/0004-637X/776/1/16

Raouafi, N. E., Patsourakos, S., Pariat, E., et al. 2016, Space Science Reviews, 201, 1, doi: 10.1007/s11214-016-0260-5

Savcheva, A., Cirtain, J., Deluca, E. E., et al. 2007, Publications of the Astronomical Society of Japan, 59, 771, doi: 10.1093/pasj/59.sp3.S771

Shen, Y. 2021, Proceedings of the Royal Society of London Series A, 477, 217, doi: 10.1098/rspa.2020.0217

Shen, Y., Liu, Y., Su, J., & Deng, Y. 2012, Astrophysical Journal, 745, 164, doi: 10.1088/0004-637X/745/2/164

Shen, Y., Liu, Y. D., Su, J., Qu, Z., & Tian, Z. 2017, Astrophysical Journal, 851, 67, doi: 10.3847/1538-4357/aa9a48

Shibata, K., & Magara, T. 2011, LRSP, 8, 6

Shibata, K., Masuda, S., Shimojo, M., et al. 1995, ApJL, 451, L83, doi: 10.1086/309688

Shibata, K., & Uchida, Y. 1986, Solar Physics, 178, 379

Shibata, K., Ishido, Y., Acton, L. W., et al. 1992, Publications of the Astronomical Society of Japan, 44, L173

Shibata, K., Nakamura, T., Matsumoto, T., et al. 2007, Science, 318, 1591, doi: 10.1126/science.1146708

Shimojo, M., Hashimoto, S., Shibata, K., et al. 1996, Publications of the Astronomical Society of Japan, 48, 123, doi: 10.1093/pasj/48.1.123

Solanki, R., Srivastava, A. K., & Dwivedi, B. N. 2020, SoPh, 295, 27, doi: 10.1007/s11207-020-1594-4

Sterling, A. C., Harra, L. K., & Moore, R. L. 2007, ApJ, 669, 1359, doi: 10.1086/520829

Sterling, A. C., & Moore, R. L. 2003, ApJ, 599, 1418, doi: 10.1086/379164

Sterling, A. C., Moore, R. L., Falconer, D. A., & Adams, M. 2015, Nature, 523, 437, doi: 10.1038/nature14556

Sterling, A. C., Moore, R. L., Falconer, D. A., & Knox, J. M. 2014, Astrophysical Journal, 788, L20, doi: 10.1088/2041-8205/788/2/L20

Sterling, A. C., Moore, R. L., Falconer, D. A., et al. 2016, Astrophysical Journal, 821, 100, doi: 10.3847/0004-637X/821/2/100

Sterling, A. C., Moore, R. L., Falconer, D. A., Panesar, N. K., & Martinez, F. 2017, Astrophysical Journal, 844, 28, doi: 10.3847/1538-4357/aa7945

Sterling, A. C., Moore, R. L., & Freeland, S. L. 2011, Astrophysical Journal, 731L, 3, doi: 10.1088/2041-8205/731/1/L3

Sterling, A. C., Moore, R. L., & Harra, L. K. 2011, ApJ, 743, 63, doi: 10.1088/0004-637X/743/1/63

Sterling, A. C., Moore, R. L., & Panesar, N. K. 2018, Astrophysical Journal, 864, 68, doi: 10.3847/1538-4357/aad550

Su, Y., Surges, V., van Ballegooijen, A., DeLuca, E., & Golub, L. 2011, ApJ, 734, 53, doi: 10.1088/0004-637X/734/1/53

Tandberg-Hanssen, E., Martin, S. F., & Hansen, R. T. 1980, SoPh, 65, 357, doi: 10.1007/BF00152799

Török, T., Panasenco, O., Titov, V. S., et al. 2011, Astrophysical Journal, 739, L63, doi: 10.1088/2041-8205/739/2/L63

Wyper, P. F., Antiochos, S. K., & DeVore, C. R. 2017, Nature, 544, 452, doi: 10.1038/nature22050

Wyper, P. F., DeVore, C. R., & Antiochos, S. K. 2018a, Astrophysical Journal, 852, 98, doi: 10.3847/1538-4357/aa9ffc

Wyper, P. F., DeVore, C. R., & Antiochos, S. K. 2019, MNRAS, 490, 3679, doi: 10.1093/mnras/stz2674

Wyper, P. F., DeVore, C. R., Karpen, J. T., Antiochos, S. K., & Yeates, A. R. 2018b, Astrophysical Journal, 864, 165, doi: 10.3847/1538-4357/aad9f7

Yang, J., Dai, J., Chen, H., Li, H., & Jiang, Y. 2018, ApJ, 862, 86, doi: 10.3847/1538-4357/aaccfd

Yokoyama, T., & Shibata, K. 1995, Nature, 375, 42, doi: 10.1038/375042a0

Young, P. R., & Muglach, K. 2014a, Solar Physics, 289, 3313, doi: 10.1007/s11207-014-0484-z

—. 2014b, Publications of the Astronomical Society of Japan, 66, 12, doi: 10.1093/pasj/psu088

Zhang, Q. M., Huang, Z. H., Hou, Y. J., et al. 2021, A&A, 647, A113, doi: 10.1051/0004-6361/202038924

Table 1. Examined Coronal Jets

Event	Date	Start	Duration	Type	Clear MF ejection?	Velocity [km s^{-1}]	MF Length (arcsec)	Notes
J1	2017 Jan 13	12:30	27	Blowout	Uncertain	14	10—15	Swirling amorphous MF expelled from JBP location with substantial horizontal movement, perhaps best visible in 304. MF material may flow out along open field, but cannot confirm this, hence it is uncertain whether the EMF is ejective or (partially) confined.
J2	2017 Jan 13	12:57	07	Uncertain	Yes	37	∼7	Measured in 171. EMF clearly appears as an erupting loop in all four channels. Measured size is of whole minifilament in 171 at 12:54 UT (∼erupting loop footpoint separation distance).
J3	2017 Jan 13	13:02	39	Uncertain	Uncertain	12	∼12	A weak jet in XRT and relatively small in size, making details hard to assess. MF eruption appears at least partially ejective and perhaps partially confined in 171, but appears to be largely confined in the other three channels. Velocity from 193; size from 193 at 12:55 UT.
J4	2017 Jan 13	13:42	≥14	Blowout	partial	52	∼20	Measured in 171. Size of whole minifilament in 171 at 13:42 is $\sim 20''$, but probably only its western half erupts.
J5	2017 Mar 6	10:58	28	Blowout	No	23	25	Confined EMF, expelled from JBP location and confined to revolving motion over neighboring magnetic lobe, as in Fig. 9; clear in all four channels. Size of minifilament measured in 304 11:06:57.
J6	2017 Mar 6	11:48	21	Standard	Partial ejection	22	∼6—10	Erupting loop MF, with at least some of the material leaking onto vertical field near loop apex; visible in all but 304; hard to see in 304, perhaps due to small size and near-limb location. Size is of EMF-loop base in 193 over ∼11:48—11:51.
J7	2017 Mar 6	11:53	15	Uncertain	Faint EMF	19	∼4—7	Maybe best in 211; too small and too near limb for 304. Small blob moving horizontally, and may leak out of spire, but hard to tell. Size is rough estimate of blob width in 211 at 11:53:45.

Table 1 *continued on next page*

Table 1 *(continued)*

Event	Date	Start	Duration	Type	Clear MF ejection?	Velocity [km s^{-1}]	MF Length (arcsec)	Notes
J8	2017 Mar 6	12:05	23	Standard	No	9	∼10	EMF appears as small feature moving horizontally at base of spire, maybe best seen in 193 and 211. Size is rough estimate of length (perhaps foreshortened) in 193 at 12:10:09.
J9	2017 Mar 6	12:37	21	Standard	Confined(?)	54	∼12	Homologous with J6. Clear erupting-loop minifilament eruption, visible in all channels, maybe best contrast in 211. Size is rough estimate of projected length measured in 211 at 12:17:45.
J10	2017 Mar 6	12:48	15	Blowout	Uncertain	15—30	∼13	Very faint minifilament erupts outward in 193, but not really visible in other channels; appears to "leak out" from apex of bright base over about 12:48 to 12:56. Measured size is that of the leaking-out structure in 193 at 12:51:09.
J11	2017 Mar 6	13:18	17	Uncertain	First confined, then leaks out	35	∼14	Clear EMF in all channels. Becomes confined at 13:19, but then leaks out the spire until at least 13:44. Size measured in 171, just prior to leak out.
J12	2017 Mar 6	13:59	8	Uncertain	No clear EMF	—	—	Faint jet in XRT, but very bright in AIA. No clear EMF. A candidate is present, especially in 211 Å] over 14:03—14:05 UT, but difficult to separate unambiguously from other surrounding outflows. Any potential EMF is likely largely hidden due to small size (bright base extent ∼12″ at 14:04:09 UT) and obscuration by spicule forest.
J13	2017 Mar 6	14:38	14	Blowout	Yes	48	∼13	Sigmoid-shaped EMF being ejected, clear in all channels sans 304. MF seems to split upon eruption. Size (linear extent) measured in 171 at 14:40:21. Velocity is of erupting west lobe of sigmoid filament over 14:40:57—14:41:57 UT.

Table 1 *continued on next page*

Table 1 *(continued)*

Event	Date	Start	Duration	Type	Clear MF ejection?	Velocity [km s^{-1}]	MF Length (arcsec)	Notes
J14	2017 Mar 6	15:42	8	Blowout	Yes	8; 22	$\sim$8	Similar to 13. Clear erupting sigmoid-shaped minifilament; visible in all channels. MF seems to split upon eruption, and only part of it is ejected. Size (linear extent) measured in 211 at 15:37:45. Slower velocity is pre-eruption expansion of east lobe of sigmoid MF over 15:34:21 - 15:37:33; faster velocity is of erupting east lobe of sigmoid MF over 14:44:09 - 15:45:33 UT.
J15	2017 Jul 4	12:59	33	Blowout	No (aborted ejection)	18	$\sim$5	EMF that is clearly confined, apparent in all channels. Velocity from 171 during eruption, over 12:55:21 - 13:02:09 UT. Size is from 171 at 12:57:55 UT, but it is likely severely foreshortened.
J16	2017 Jul 4	16:07	19	Standard	No (revolving)	33	$\sim$15	Clear confined EMF, best seen in 304. Velocity from 304 during eruption, over 16:09:57 - 16:11:57 UT. Size is $15''$ from 304 at 16:12:21 UT, likely severely foreshortened.
J17	2018 Apr 3	14:19	43	Uncertain	Mainly confined (but perhaps leaks out)	33	$\sim$15	Confined EMF, but some cool material may leak out near apex of MF's eruption. Best visible in 193 and 211 as short extended silhouette, more faintly visible in 171; not apparent in 304.. Velocity is from 211 over 14:18:09 - 14:19:45 UT. Size is from 211 at 14:18:33.
J18	2018 Apr 3	14:52	17	Blowout	Partial ejection	23, 26	$\sim$18	EMF first confined, but then part of it ejecting outward. Clear in all channels. Velocities and size from 171. Slower velocity is MF moving up onto large lobe, faster velocity is that of an erupting strand. Size of $\sim 18''$ is from 15:04:57, when MF is seen in profile and so thus perhaps with minimal foreshortening.

Table 1 *continued on next page*

Table 1 *(continued)*

Event	Date	Start	Duration	Type	Clear MF ejection?	Velocity [km s^{-1}]	MF Length (arcsec)	Notes
J19	2018 Apr 3	15:23	$\gtrsim$37	Blowout	Faint, and obscured by haze	$\lesssim$30	∼28	Weak X-ray jet. Also hazy in AIA, but there is a clear EMF, and it is probably ejective, erupting over 15:32 - 15:57, weakly detectable in all channels. Seems to be a non-consolidated MF. Derived velocity, from 171, is from a fast-moving easily discernible substructure that perhaps moves faster than other parts of the MF. Size is that of the base of the EMF structure in 171.
J20	2018 Apr 3	16:35	12	Blowout	Mainly confined	∼11-15	∼25	Homologous with J18. Same type of MF, and same type of ”crawl up” is visible in all channels. There is some partial ejection over 16:41-16:45 UT. Derived velocity from 171 is of MF moving up to apex of large lobe. Size is from 171 when it is near the apex of that lobe.
J21	2018 Apr 3	16:58	22	Blowout	Yes	∼10-13	∼15—20	Homologous with J17. Clear erupting feature visible in all channels, but best visible as a (subtle) dark EMF feature in 193 and 211. Velocity is of pre-eruption MF slow rise from 193. Size is length in 193, perhaps seen in profile (and so reduced foreshortening).

Table 2. Blowout/Standard Jets, and Erupting Minifilaments

Jet	Type		EMF's Degree of Jet Base Confinement	
J1	Blowout		Uncertain	
J4	Blowout		Partial	
J5	Blowout		Confined	
J10	Blowout		Uncertain	
J13	Blowout		Ejective	
J14	Blowout		Ejective	
J15	Blowout		Confined	
J18	Blowout		Partial	
J19	Blowout		Uncertain	
J20	Blowout		Confined	
J21	Blowout		Ejective	
J6	Standard		Partial	
J8	Standard		Confined	
J9	Standard		Uncertain	
J16	Standard		Partial	
J2	Uncertain	(Spire between narrow and broad.)	Ejective	
J3	Uncertain	(Borderline too small and weak for assessment.)	Uncertain	
J7	Uncertain	(Narrow bright spire, with faint broader component.)	Ejective	
J11	Uncertain	(Too faint for clear determination.)	Mixed	(First confined, then ejective.)
J12	Uncertain	(Narrow bright spire, with possible faint broad component.)	None	(Suspected, but cannot be confirmed due to faintness and small size.)
J17	Uncertain	(Spire between narrow and broad.)	Confined	

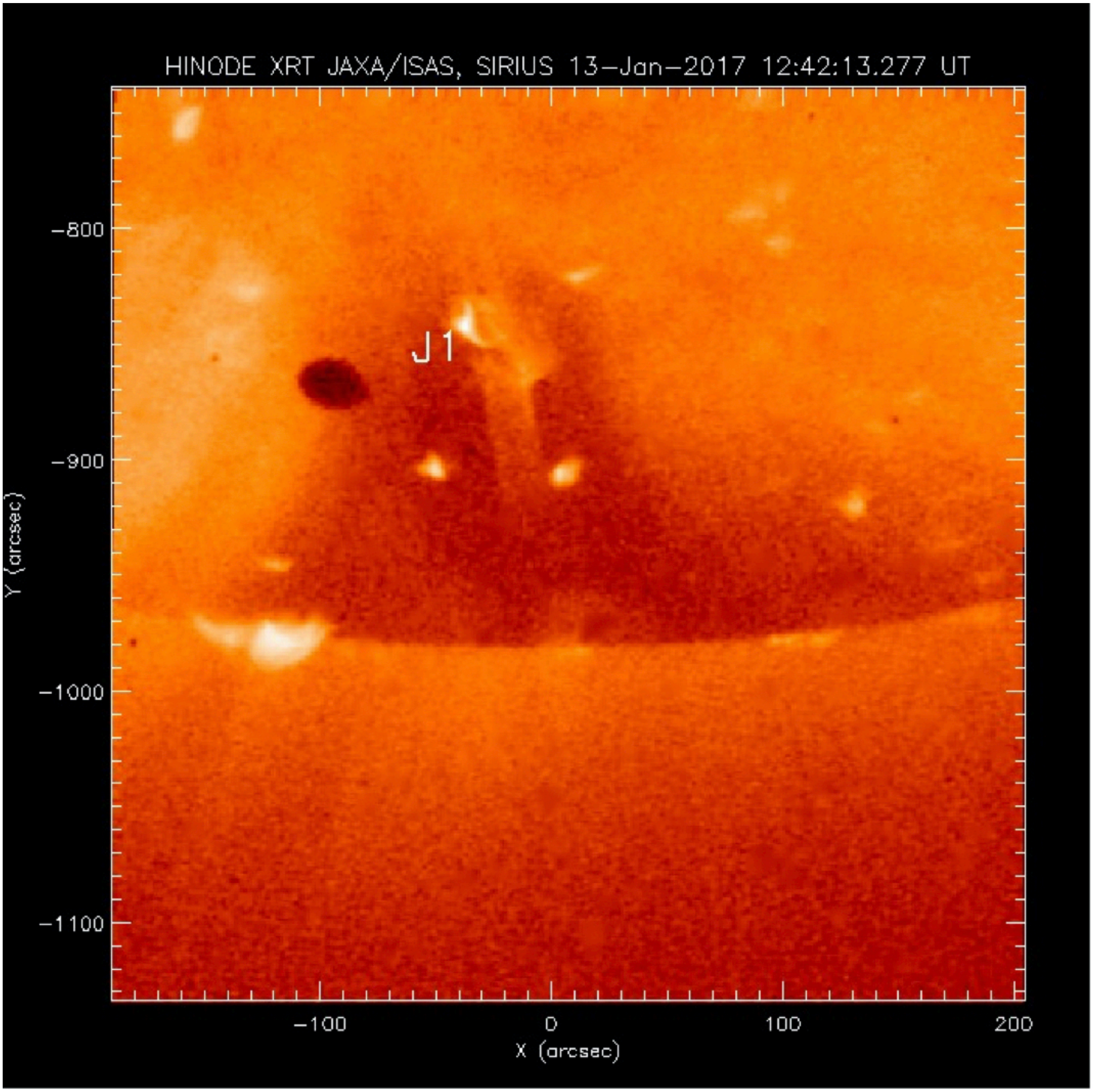

Figure 1. A soft X-ray image from the *Hinode* XRT instrument's Al Poly filter, of the south polar coronal hole region on 2017 January 13. One of the jets of Table 1, labeled J1, is in progress. North is up and west is to the right in this and in all other solar images and animations of this paper. The dark oval at about (-80,-870), and similar smaller patches and spots, are artifacts. The accompanying animation shows the XRT movie for this period, covering 2017 January 13 over 12:00:36—13:58:02 UT. It is constructed by performing a running sum of every two consecutive images, and is presented as a full-cadence (60 s) running-sum movie. The movie plays twice, first showing Jets J1—J4 labeled as they happen, and then again without labels. The entire movie runs for 12 s.

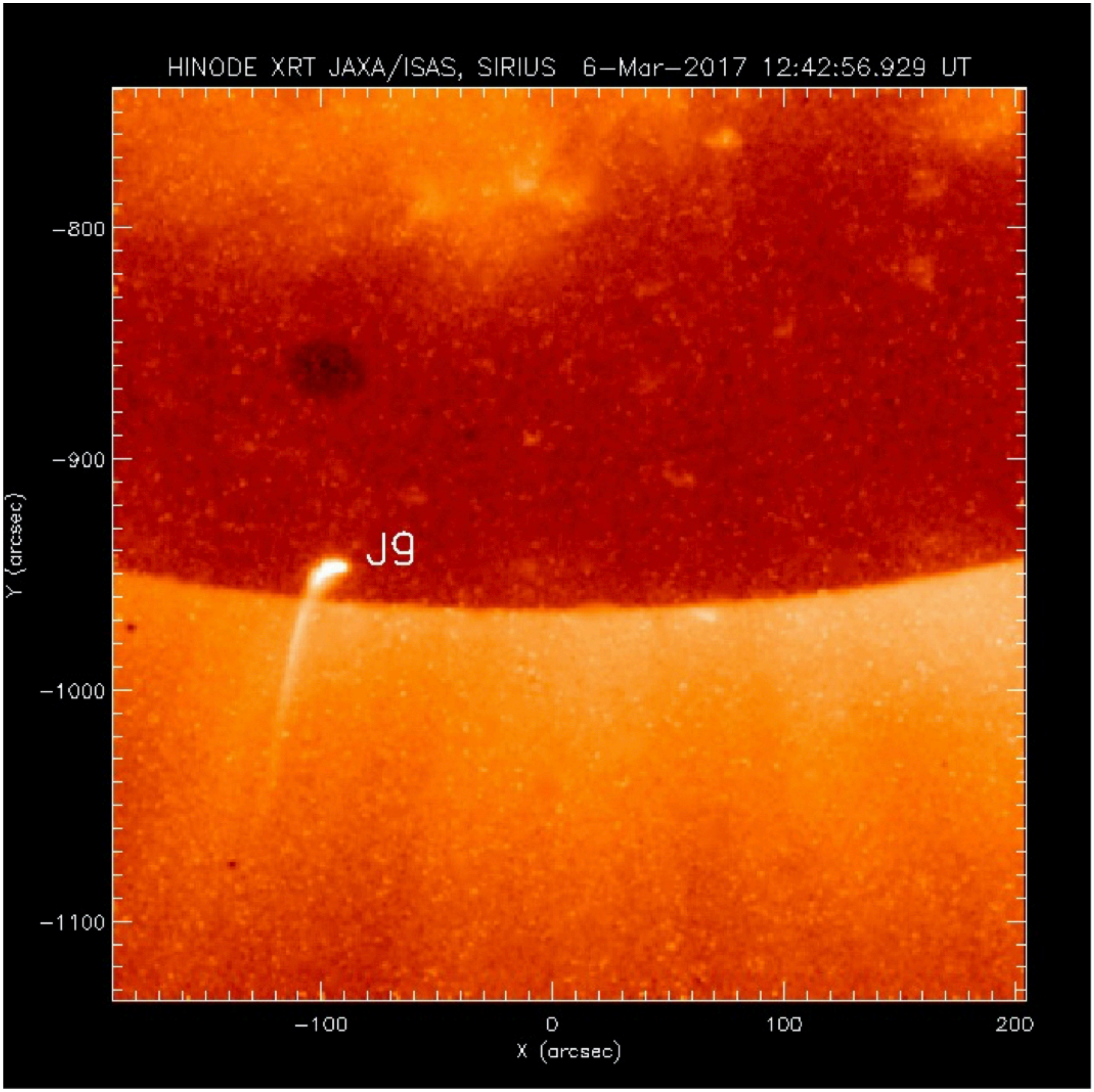

Figure 2. Similar to Fig. 1, but showing the south polar coronal hole region on 2017 March 6, at a time when jet J9 of Table 1 is in progress. The dark oval at about (-80,-870), and similar smaller patches and spots, are artifacts. The animation covers 2017 March 6, over 10:34:30—15:58:06 UT. It is constructed by performing a running sum of every two consecutive images, and is presented as a full-cadence (60 s) running-sum movie. The movie plays twice, first showing Jets J5—J14 labeled as they occur, and then again without labels. The entire movie runs for ∼31 s.

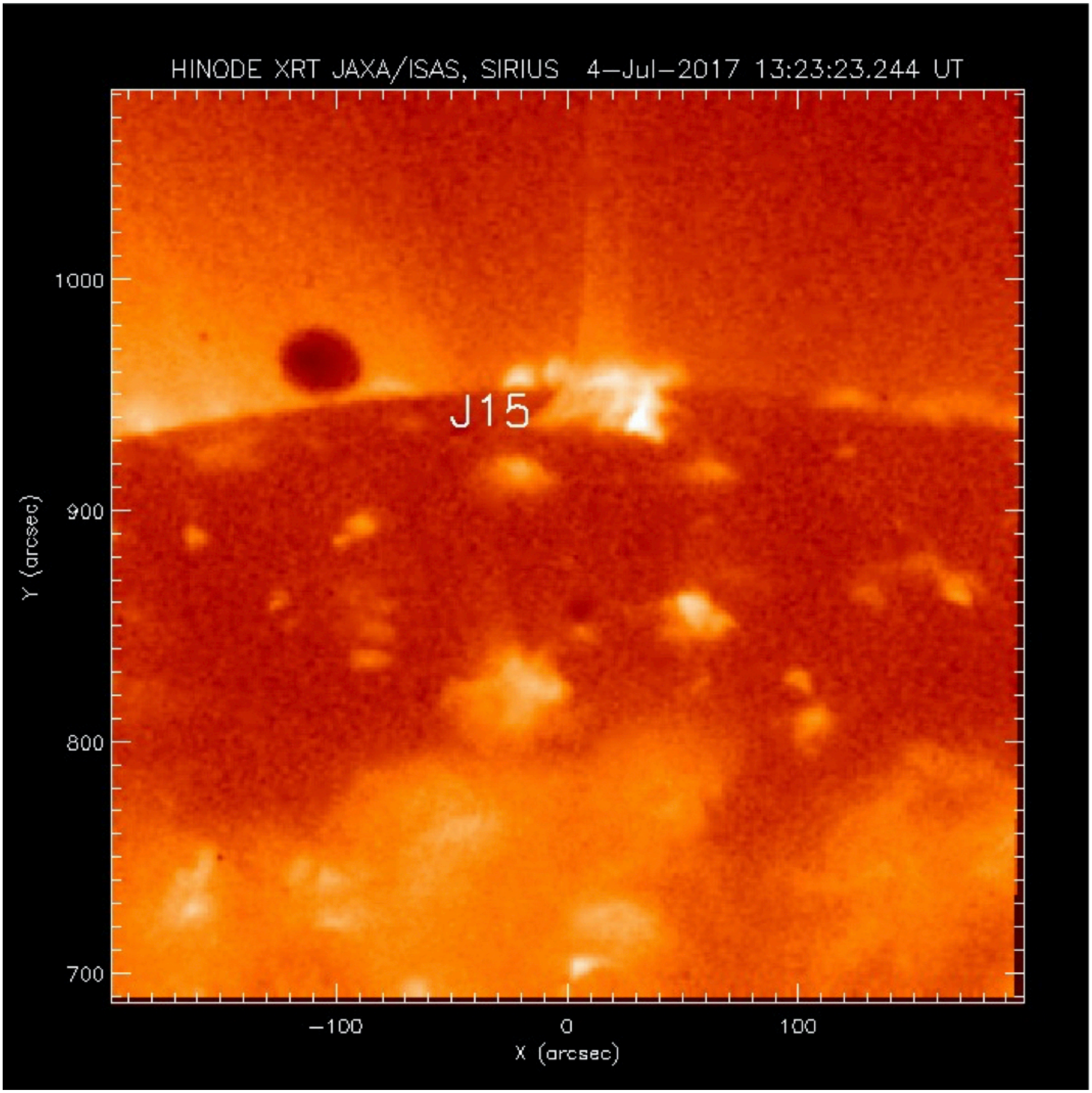

Figure 3. Similar to Figs. 1 and 2, but showing the north polar coronal hole region on 2017 July 4, at a time when jet J15 of Table 1 is in progress. The dark oval at about (-100,970), and similar smaller patches and spots, are artifacts. The animation covers 2017 July 4 over 12:45:05—16:33:20 UT. It is constructed by performing a running sum of every two consecutive images, and is presented as a full-cadence (60 s) running-sum movie. The movie plays twice, first showing Jets J15 and J16 labeled as they occur, and then again without labels. The entire movie runs for ∼29 s.

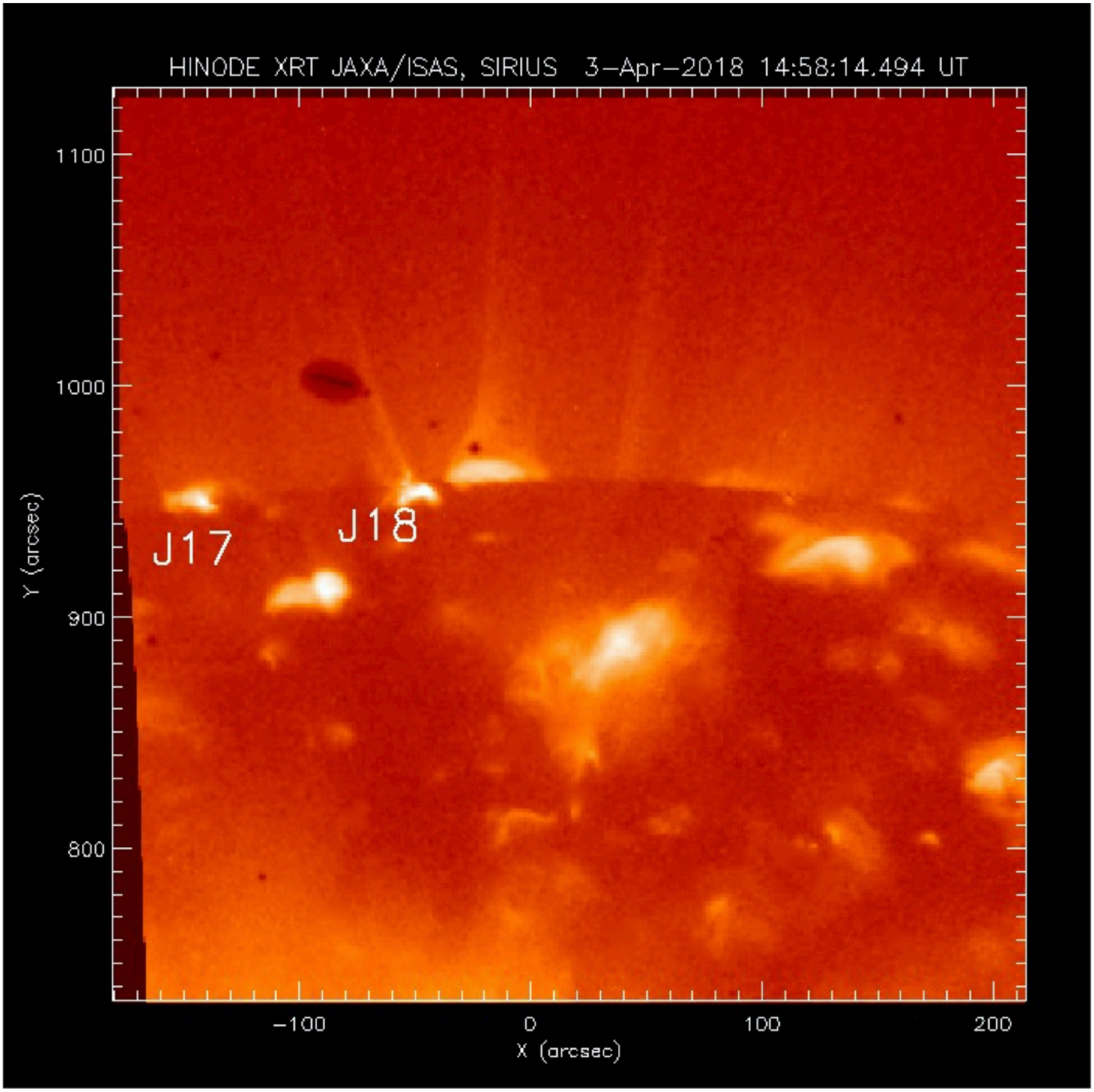

Figure 4. Similar to Figs. 1, 2, and 3, but showing the north polar coronal hole region on 2018 April 3, at a time when Table 1 jet J17 is about to end, and jet J18 is in progress. Also apparent in this image is a jet at the limb near $x = 0$; although prominent in X-rays, we feared that it is too close to the limb for a reliable analysis of the corresponding AIA images, and therefore we did not include it in our study. The dark oval at about (-100,970), and similar smaller patches and spots, are artifacts. The animation covers 2018 April 3, over 13:48:58—17:36:02 UT. This video is constructed by performing a running sum of every two consecutive images, and is presented as a full-cadence (60 s) running-sum movie. The movie plays twice, first showing Jets J17 and J21 labeled as they occur, and then again without labels. The entire movie runs for ∼30 s.

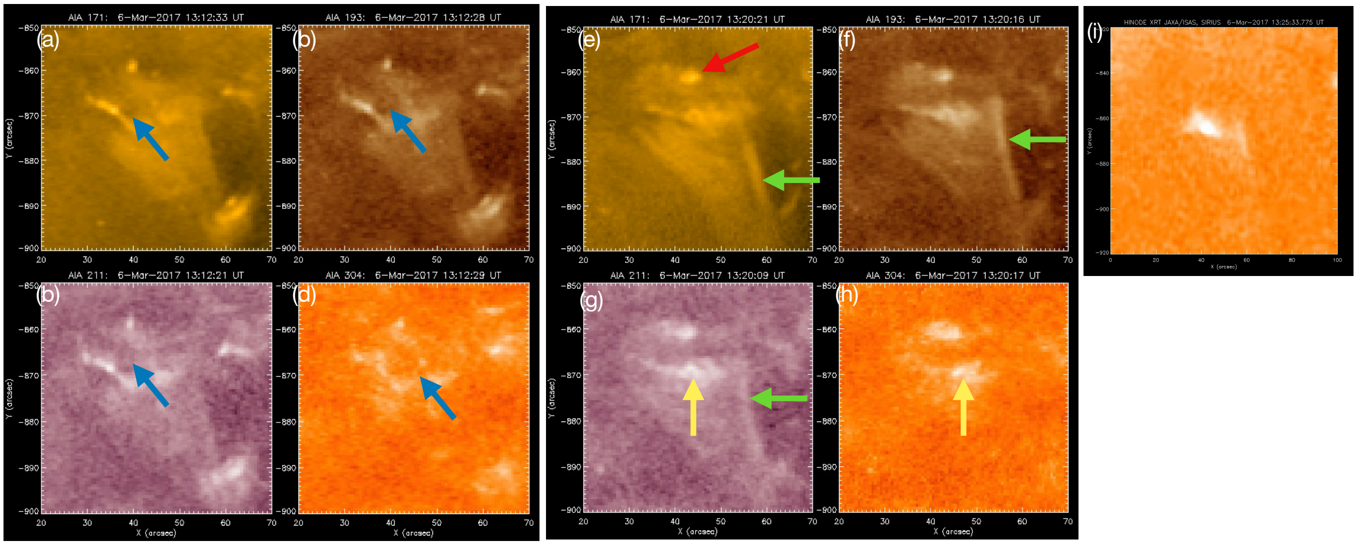

Figure 5. AIA images and an XRT closeup of Table 1 jet J11. The AIA images are in 171, 193, 211, and 304 Å, showing the jet at two different times, near 13:12 UT (left four panels) and near 13:20 UT (right four panels, on 2017 March 6; details of each frame are provided in the labels at the top of the panels. Blue arrows show an erupting minifilament (EMF) in absorption. By the time of the right-side panels the minifilament has erupted out of the field of view. The red arrow shows the location of the JBP, corresponding to the location between M2 and M3 in Fig. 1 of Sterling et al. (2018) (and in Fig. 9 below). The yellow arrows show the location of the large lobe, corresponding to the location between M1 and M2 in those schematics. It has brightened due to the EMF flux rope's external reconnection. In the left four panels, this lobe is partially obscured by the erupting cool minifilament in the foreground. Green arrows point to the jet spire. Panel (i) shows a zoomed-in XRT view of the jet (axis ranges are different from those of the AIA panels). The animation covers 2017 March 6, over approximately 12:50—13:50 UT for AIA, and over 13:08—13:50 UT for XRT. The videos are constructed by performing a running sum of every two consecutive images; the AIA videos are presented as full-cadence (12 s) running-sum movies, while the XRT video is presented as a running-sum movie of cadence ∼60 s. The entire five-panel movie runs for ∼7 s.

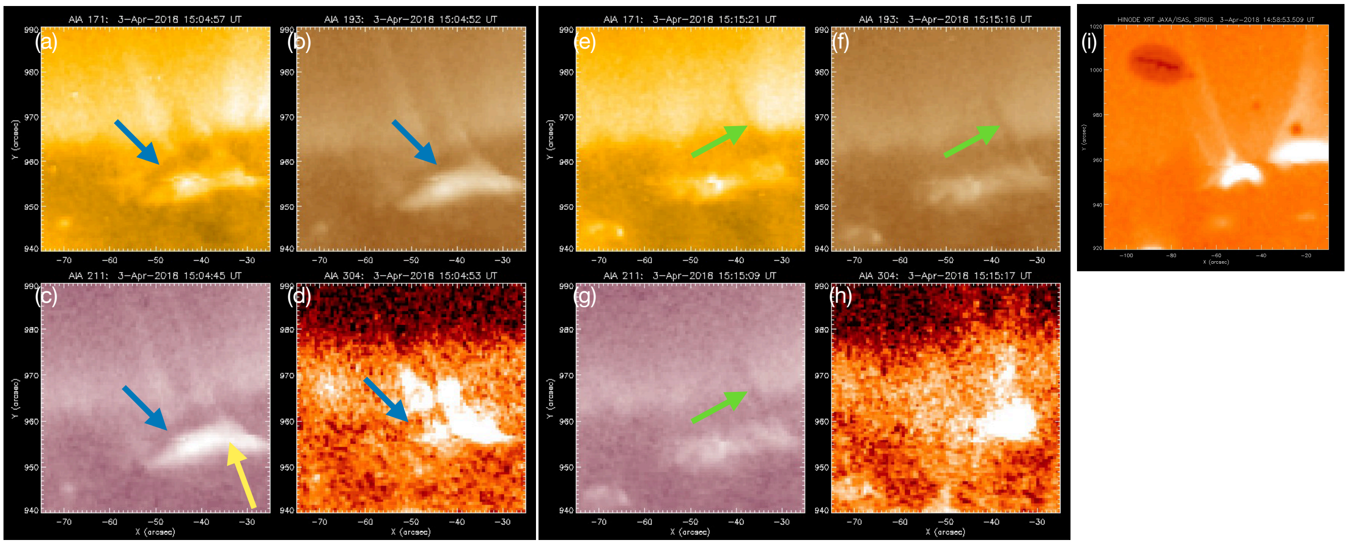

Figure 6. AIA images and an XRT closeup of Table 1 jet J18. The AIA images are in 171, 193, 211, and 304 Å, showing the jet at two different times, near 15:04 UT (left four panels) and near 15:15 UT (right four panels, on 2018 April 3; details of each frame are provided in the labels at the top of the panels. Arrow colors are as in Fig. 5. From the accompanying animation, the minifilament initially resides on the far side of the big lobe, and at the time of panels (a)—(d) it has crawled up to the top of that lobe. In panels (e)—(h), the minifilament is erupting outward; in this case, the green arrows show a strand of dark minifilament material in the spire, while brighter strands of the spire are apparent in the XRT movies (Figs. 4 and 6). Panel (i) shows a zoomed-in XRT view of the jet (axis ranges are different from those of the AIA panels); the large dark oval, and similar smaller patches and spots, are artifacts. The animation covers 2018 April 3, over approximately 14:34—15:20 UT. The videos are constructed by performing a running sum of every two consecutive images; the AIA videos are presented as full-cadence (12 s) running-sum movies, while the XRT video is presented as a running-sum movie of cadence ∼30—60 s. The entire five-panel movie runs for ∼7 s.

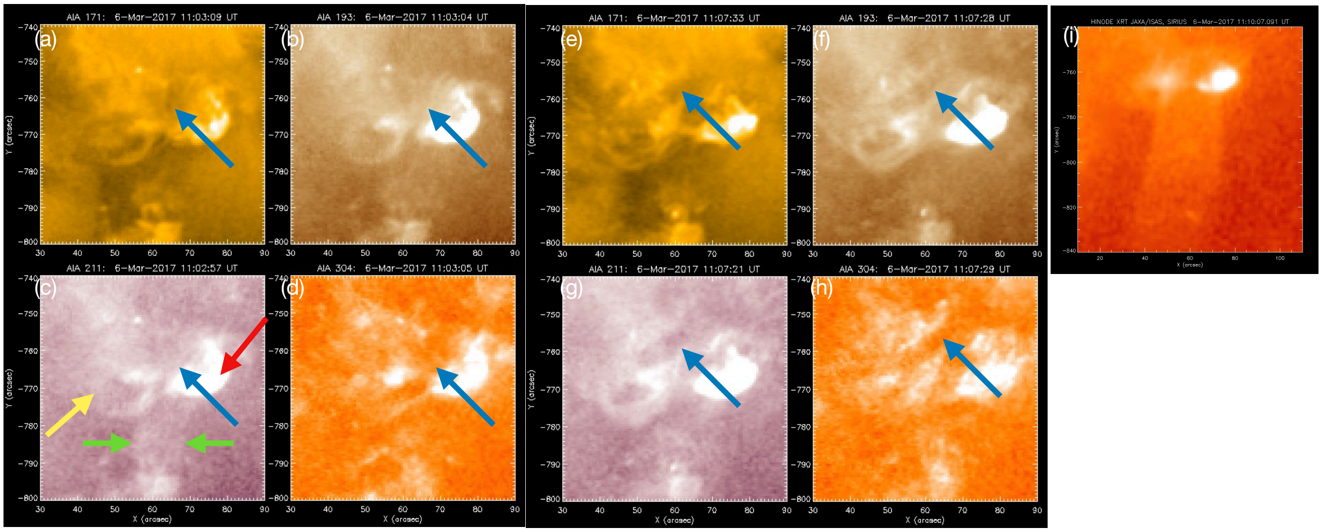

Figure 7. AIA images and an XRT closeup of Table 1 jet J5. The layout is as in Figs. 5 and 6, but for event J5 near 11:03 UT (left four panels) and near 11:07 UT (right four panels, on 2017 March 6. Arrow colors are as in Fig. 5. From the accompanying animation, in this case the minifilament initially resides on the southwest side of the M1—M2 lobe of Fig. 9 (below), erupts and rotates over that lobe to its northeast side. Apparently it erupts and largely remains trapped in the base of the region as depicted in Fig. 9 (at least until ∼11:09 UT, after which time it we cannot determine with certainty whether it remains confined or ejects outward). Panel (i) shows a zoomed-in XRT view of the jet (axis ranges are different from those of the AIA panels). The animation covers 2017 March 6, over approximately 10:34—11:30 UT. The videos are constructed by performing a running sum of every two consecutive images; the AIA videos are presented as full-cadence (12 s) running-sum movies, while the XRT video is presented as a running-sum movie of cadence ∼60 s. The entire five-panel movie runs for ∼9 s.

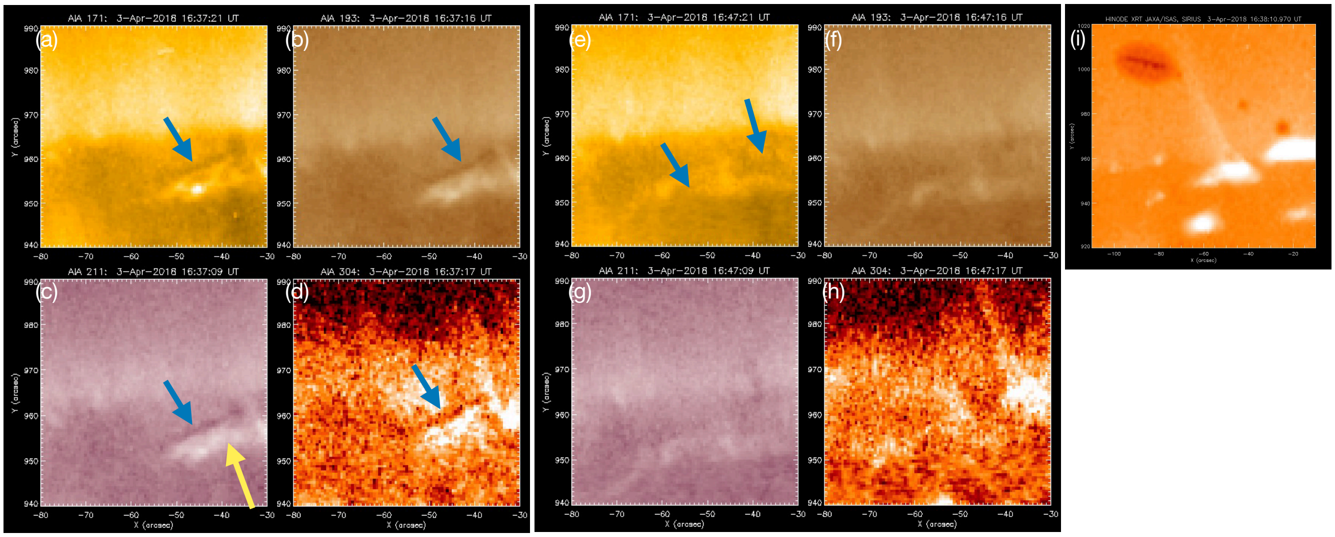

Figure 8. AIA images and an XRT closeup of Table 1 jet J20. The layout is as in Figs. 5—7, but for jet event J20 near 16:37 UT (left four panels) and near 16:47 UT (right four panels, on 2017 March 6. Arrow colors are as in Figs. 5—7. From the accompanying animation, this event is largely homologous with jet J18 (Fig. 6), with the minifilament initially residing on the far side of that lobe, and at the time of panels (a)—(d) it has crawled up to the top of the lobe. In this case however, more of the filament remains near the solar surface than in the jet J18 case, with some of the minifilament rotating onto the near side of the lobe in panels (e)—(h) (blue arrows). Thus, this is similar to the XRT-jet-causing minifilament eruption of Fig. 7 (at least for much of its life), with the minifilament largely remaining trapped in the base. Apparently it erupts and remains trapped in the jet base, as depicted in Fig. 9. Panel (i) shows a zoomed-in XRT view of the jet (axis ranges are different from those of the AIA panels); the large dark oval, and similar smaller patches and spots, are artifacts. The animation covers 2018 April 3, over approximately 16:25—16:55 UT. The videos are constructed by performing a running sum of every two consecutive images; the AIA videos are presented as full-cadence (12 s) running-sum movies, while the XRT video is presented as a running-sum movie of cadence ∼30—60 s. The entire five-panel movie runs for ∼5 s.

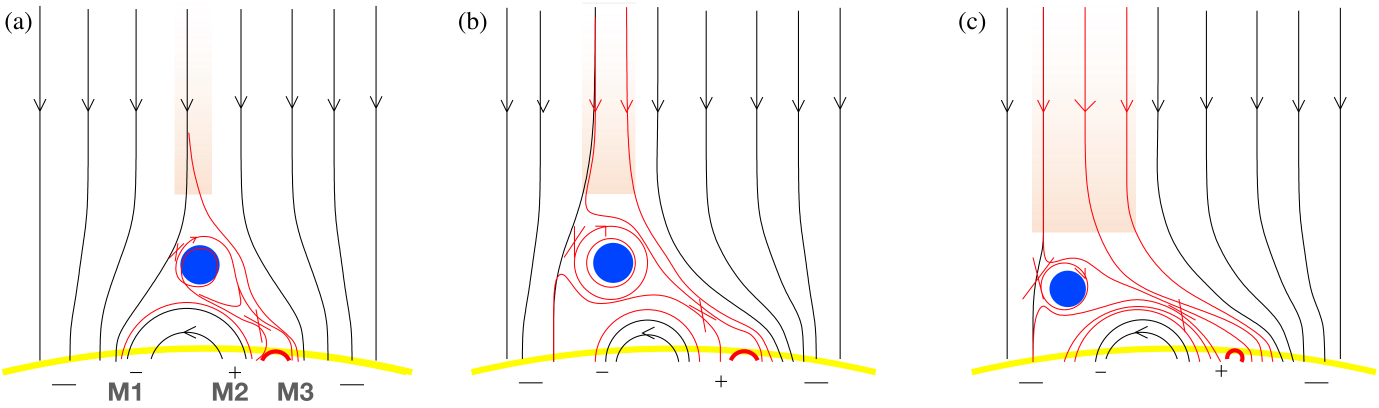

Figure 9. Schematic picture of how some wide-spire jets work according to the minifilament eruption model, where the jet is made by a largely confined minifilament eruption. (These would be called "blowout jets" based on the Moore et al. 2010 and 2013 criteria based on the broad X-ray spire, despite the EMF's flux rope being largely confined.) Panel (a) is the same as panel (b) in Fig. 1 of Sterling et al. (2018). Here, panels (a), (b), and (c) together depict that the minifilament flux rope largely passes over the apex of the M1—M2 magnetic lobe, with a minimum amount of the cool material escaping into the jet spire, much less than it is doing in the schematic of panel (c) of Sterling et al. (2015). Each red field line indicates a newly reconnected field line. The shaded region widens along with the moving minifilament at the base, widening with time away from from the JBP of the M2—M3 lobe; this occurs as the outside of the confined EMF's flux rope progressively reconnects with field lines to the left in this perspective.

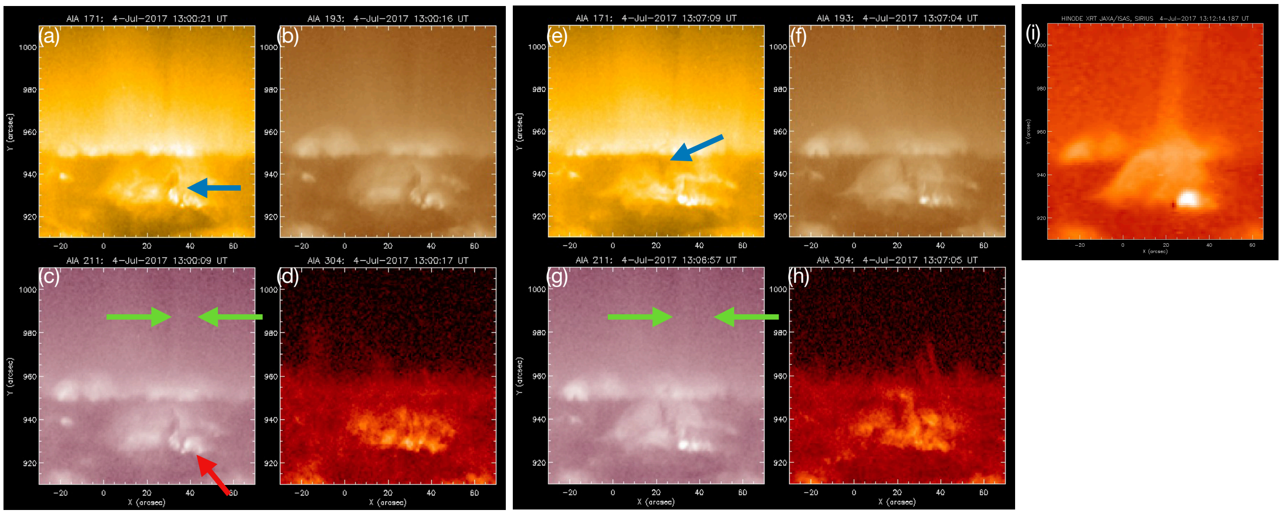

Figure 10. AIA images and an XRT closeup of Table 1 jet J15. The layout is as in Figs. 5—8, but for jet event J15, near 13:00 UT (left four panels) and near 13:07 UT (panels (e)—(h)), on 2017 July 4. Arrow colors are as in Figs. 5—8. This is an example of a confined minifilament eruption of a different nature than those of Figs. 7 and 8. In those previous cases the EMF's flux rope had only enough energy to stay close to (ride on top of) the magnetic lobe M1—M2 of Fig. 9 (although in the case of Fig. 7 we cannot determine whether the minifilament ejects outward later in its evolution). In this case, the EMF breaks free of the base region and starts to erupt into the higher corona, as in panels (b) and (c) of the schematic in Sterling et al. (2015). But its outward movement is largely stopped, presumably due to strong confining enveloping and surrounding field, and then returns to the surface. This has been observed in confined large-scale filament eruptions (e.g., Ji et al. 2003; Sterling et al. 2011). Panel (i) shows a zoomed-in XRT view of the jet (axis ranges are different from those of the AIA panels). The animation covers 2017 July 4, over approximately 12:41—13:30 UT. The videos are constructed by performing a running sum of every two consecutive images; the AIA videos are presented as full-cadence (12 s) running-sum movies, while the XRT video is presented as a running-sum movie of cadence ∼30 s. The entire five-panel movie runs for ∼5 s.

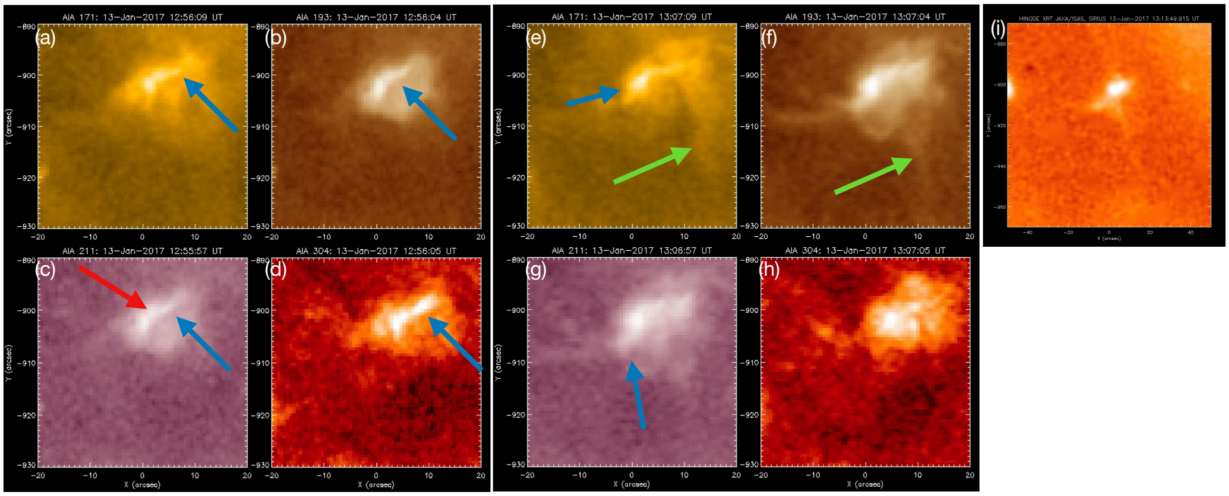

Figure 11. AIA images and an XRT closeup of Table 1 jet J3. The layout is as in Figs. 5—8, and Fig. 10, but for jet event J3, near 12:56 UT (left four panels) and near 13:07 UT (right four panels, on 2017 January 13. Arrow colors are as in Figs. 5—8 and 10. This is an example of a case of a jet-base EMF that we judged to be "difficult to identify." From the accompanying animation, we strongly suspect the feature indicated by the blue arrows is a faint EMF. (Part of that EMF appears perhaps to be ejective, near the location of the green arrow in (e), but this cannot be confirmed in the other channels; see text.) Fundamentally it follows the pattern of the schematic in Sterling et al. (2015) and Sterling et al. (2018), where our perspective here is viewing that schematic from the right-hand side; that is, we are seeing the minifilament face-on as it rises over the M1—M2 magnetic lobe in the Sterling et al. (2018) schematic. In the video, the EMF reaches near the lobe's apex at about 13:00 UT, and then it starts to expand in the SE—NW direction until about 13:20 UT, presumably as it reconnects with surrounding coronal field as depicted in the basic schematic of Sterling et al. (2015). In this case, the cool minifilament does not strongly continue to erupt radially from the Sun, as pictured in the Sterling et al. (2015) schematic, but remains partially trapped in the base region of the jet, as schematically depicted in Fig. 9. Panel (i) shows a zoomed-in XRT view of the jet (axis ranges are different from those of the AIA panels). The animation covers 2017 January 13, over approximately 12:39—13:59 UT for AIA, and over approximately 12:57—13:50 UT for XRT. The videos are constructed by performing a running sum of every two consecutive images; the AIA videos are presented as full-cadence (12 s) running-sum movies, while the XRT video is presented as a running-sum movie of cadence ∼60 s. The entire five-panel movie runs for ∼10 s.